An adaptive multiresolution semi-intrusive scheme for UQ in compressible fluid problems

Rémi Abgrall, Pietro Marco Congedo, Gianluca Geraci, Gianluca Iaccarino

An adaptive multiresolution semi-intrusive scheme for UQ in compressible fluid problems

Rémi Abgrall, Pietro Marco Congedo, Gianluca Geraci, Gianluca Iaccarino

RESEARCH REPORT
N° 8688
January 2015
Project-Teams Cardamom

ISSN 0249-6399 ISRN INRIA/RR--8688--FR+ENG

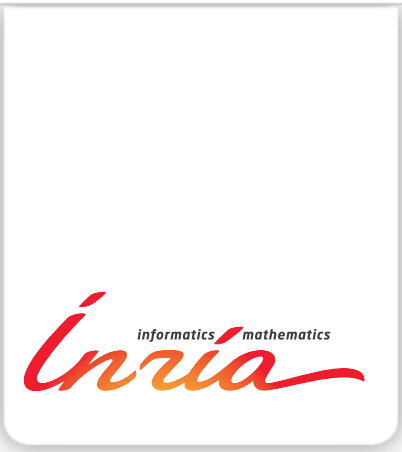

An adaptive multiresolution semi-intrusive scheme for UQ in compressible fluid problems

Rémi Abgrall, Pietro Marco Congedo, Gianluca Geraci, Gianluca Iaccarino

Project-Teams Cardamom

Research Report n° 8688 — January 2015 — 49 pages

Abstract: This paper deals a multiresolution strategy applied to a semi-intrusive scheme recently introduced by the authors in the context of uncertainty quantification (UQ) analysis for compressible fluids problems. The mathematical framework of the multiresolution framework is presented for the cell-average setting and the coupling with the existing semi-intrusive scheme is described from both the theoretical and practical point-of-view. Some reference test-cases are performed to demonstrate the convergence properties and the efficiency of the overall scheme: the linear advection problem for both smooth and discontinuous initial conditions, the inviscid Burgers equation and the 1D Euler system of equations to model an uncertain shock tube problem obtained by the well-known Sod shock problem. For all the cases presented, the convergence curves are computed with respect to semi-analytical solutions obtained for the stochastic formulation of the test cases. In the case of the shock tube problem, an original technique to obtain a reference high-accurate numerical stochastic solution has also been developed.

Key-words: Uncertainty Quantification, adaptive semi-intrusive scheme (aSI), linear advection, Burgers equation, Euler equations, shock tube

RESEARCH CENTRE BORDEAUX – SUD-OUEST

351, Cours de la Libération
Bâtiment A 29
33405 Talence Cedex

Un schma semi-intrusif adaptatif pour la quantification des incertitudes dans des problmes d'coulements compressibles

Résumé : Ce papier est focalis sur une stratgie multi-rsolution applique un schma semi-intrusif introduit par les auteurs dans le cadre d'une analyse de quantification des incertitudes pour les fluides compressibles. Le cadre mathmatique est prsent pour un "cell-average setting". Des cas-tests de rfrence sont raliss pour dmontrer les proprits de convergence de la mthode et l'efficacit du schma global: un problme d'advection linaire, une quation de Burgers et un systme d'quations d'Euler pour rsoudre un problme de tube choc stochastique. Pour tous les cas prsents, les courbes de convergence sont calcules par rapport la solution semi-analytique obtenue pour la formulation stochastique des cas-tests.

Mots-clés : Quantification d'incertitude, schema adaptatif semi-intrusive (aSI), advection linaire, quation de Burgers, tube choc.

Contents

1 Introduction and motivation

In recent years, the scientific numerical community faced a new challenge, the effect and propagation of uncertain parameters in the numerical models. Nowadays, the attention is focused not only on the accurate solution of the equations, but also on the effect of uncertain parameters in boundary or initial conditions and in the model.

Among the non-intrusive approaches, *i.e.* where uncertainties are quantified practically by making multiple calls to a deterministic code, several methods are commonly employed: Monte Carlo family of techniques [1], the collocation family [2] and the non-intrusive Galerkin projection methods. This last family of methods has been introduced for the first time by Ganem and Spanos [3] for the analysis of structural dynamics systems and has been generalized by Xiu and Karniadakis [4] to general probability distributions. Actually, the non-intrusive Galerkin projection represents the state-of-the art of the stochastic analysis for systems with a smooth response surface due to its spectral convergence property.

The Galerkin projection is also the most important technique in order to manage intrusively the uncertainty propagation into a numerical code. In practice, this means that it is possible to obtain an equivalent set of governing equations for the coefficients of a truncated polynomial representation of the quantities of interest [5]. Then, the number of equations is related to the number of coefficients employed in the polynomial expansion, and the numerical code should be deeply modified. In many cases, this leads to complex problems regarding the generality of the approach when *ad hoc* solvers are proposed [6]. More recently, Abgrall and Congedo proposed a novel semi-intrusive approach

that extend in a straightforward and natural way, the representation of the variables in the physical space also along the stochastic space [7]. This approach leads to a very flexible scheme able to handle whatever form of probability density function even time varying and discontinuous. One of the prominent advantage of this kind of approach is the possibility to extend in an easier way an existing deterministic code to its stochastic counterparts.

Following the general idea of a semi-intrusive propagation of the uncertainties, recently, Abgrall et al. [8, 9, 10] introduced a point-value setting in the multiresolution (MR) framework to represent data in the stochastic space. The multiresolution representation of data permits to increase the efficiency of the numerical code for the solution of stochastic partial differential equations. The idea of introducing the MR representation of data, in the context of stochastic problem, is not totally new. In [5], a multiresolution basis is employed to represent the solution of a partial differential equations after fixing the physical coordinate. This representation is very efficient but limited to the case where the stochastic representation is used at a fixed physical location. To overcome this issue, more recently, Tryoen et al. introduced in [6] a multiresolution wavelets representation in the context of intrusive Galerkin projections. However, the Galerkin approach presented remains very problem-dependent. In fact, using a Roe-type solver demands the computation of the eigenstructure of the Roe matrix explicitly; this can be very complex. Moreover, *ad hoc* entropy fix should be adopted, thus increasing the numerical cost associated to the representation of discontinuous solution [11]. This original approach has been further improved to obtain a more efficient scheme employing a multiresolution adaptive strategy [12]. However, this approach is limited by the spatial and time discretization accuracy (only first order) that could dominate the overall accuracy. Moreover, the approach proposed by Abgrall et al [8, 9, 10] has the advantage to remain very general, not limited from the order of the spatial and time discretization, from the probability density function (that can be even discontinuous and time varying) and, eventually, from the geometry of the stochastic space in the case of multidimensional problems.

In this paper, the MR is extended to the cell-average framework and the representation is implemented in the semi-intrusive scheme [7]. Thanks to its intrinsic capability to manage discontinuous responses, the semi-intrusive methods represents a promising alternative to the Galerkin projection techniques for all the applications where the system is dominated by shocks, as for example in computational fluid dynamics for transonic flows.

In this paper, we demonstrate the advantages of the introduction of a real-time adaptivity in the stochastic space, by following the evolution of the solution in the overall physical and stochastic space. This is shown by comparing the accuracy, at a fixed computational cost, with and without the adaptivity based on the MR framework on the original SI scheme. Different reference test-cases are performed for which the reference solution can be obtained in an analytical or semi-analytical approach.

This paper is organized as follows. In section 2, the mathematical setting for the stochastic differential equation is given. Section 3 illustrates the multiresolution framework of Harten, generalized for the stochastic space, where a cell-average setting is chosen. In particular the Truncate and Encode algorithm is presented in section 3.1 where the representation of the discrete data is obtained from the coarsest level towards the finest. The semi-intrusive scheme is

briefly sketched in section 4 where the formulation is detailed for the MUSCL-Hancock method. The overall formulation of the adaptive semi-intrusive scheme is presented in 5. Several numerical results are presented in section 6. In particular, the introduction of the adaptive representation of data in the stochastic space is demonstrated to improve the spatial convergence and to cure the staircase approximation phenomenon with respect to an equivalent not adapted solution. The linear advection equation, the inviscid Burgers equation and an uncertain version of the Sod shock tube are performed as test-cases. Concluding remarks are reported in §7.

2 Uncertainty quantification for partial differential equations

In this section, we introduce the mathematical setting, used for the UQ analysis in the context of partial differential equations. Let us consider an output of interest $u(\mathbf{x}, t, \boldsymbol{\xi}(\omega))$ depending from the physical space $\mathbf{x} \in \Omega \subset \mathbb{R}^{n_d}$, the time $t \in T$ and a vector of parameters $\boldsymbol{\xi} \in \Xi$ where Ξ is the sample space. The output of interest u can be a conserved (or primitive, or another flow variable) variable of a system of conservation laws.

We suppose that the output of interest is governed by an algebraic or differential operator $\mathcal{L}$ with a source term $\mathcal{S}$:

$$\mathcal{L}(\mathbf{x}, t, \boldsymbol{\xi}(\omega); u(\mathbf{x}, t, \boldsymbol{\xi}(\omega))) = \mathcal{S}(\mathbf{x}, t, \boldsymbol{\xi}(\omega)). \tag{1}$$

Initial and boundary conditions, that could depend from the parameter vector $\boldsymbol{\xi}$, should be provided for a well-posed problem. Both the operators $\mathcal{L}$ and the source term $\mathcal{S}$ are defined on the domain $\Omega \times T \times \Xi$.

Let us define a measurable space (Ξ, Σ, p) where Σ is its $\sigma-$algebra of events and p a probability measure with the following properties:

- $p(A) \geq 0$ for all $A \in \Sigma$;
- Countable additivity: if $A_i \in \Sigma$ are disjoint sets then $p(\bigcup_i A_i) = \sum_i p(A_i)$;
- as probability measure p is normalized on Ξ: $p(\Xi) = 1$.

The $\mathbb{R}^d-$valued random variable $\boldsymbol{\xi}$ specifies a set of events with a corresponding probability. More formally, the random variable $\boldsymbol{\xi}$ is a measurable function that maps the measurable space (Ξ, Σ, p) to another measurable space, the Borel $\mathcal{B}^d$ $\sigma-$algebra of the real space $(\mathbb{R}^d, \mathcal{B}^d, \mathbb{P})$. There is some set of events ω, that $\boldsymbol{\xi}$ maps to an output event $A \in \mathcal{B}^d$ with the probability of occurrence of A, $\mathbb{P}(A)$ equal to the probability of ω:

$$\mathbb{P}(A) = p(\boldsymbol{\xi}^{-1}(A)) = p(\omega : \boldsymbol{\xi}(\omega) \in A). \tag{2}$$

As usual in the literature, we consider that $\mathbb{P}(A) = p(\boldsymbol{\xi} \in A) = p(\boldsymbol{\xi})$.

The aim of UQ analysis is to find statistical quantities of the solution $u(\mathbf{x}, t, \boldsymbol{\xi})$, the statistical moments or the probability distribution.

Assuming $u(\boldsymbol{\xi}) \in L_2(\Xi, p)$, mean and variance can be computed as follows:

$$\begin{aligned} \mathcal{E}(u, \mathbf{x}, t) &= \int_\Xi u(\mathbf{x}, t, \boldsymbol{\xi}) p(\boldsymbol{\xi}) \mathrm{d}\boldsymbol{\xi} \\ \mathrm{Var}(u, \mathbf{x}, t) &= \int_\Xi \left(u(\mathbf{x}, t, \boldsymbol{\xi}) - \mathcal{E}(u)\right)^2 p(\boldsymbol{\xi}) \mathrm{d}\boldsymbol{\xi}. \end{aligned} \tag{3}$$

3 The cell-average multiresolution setting

In this section, the multiresolution framework in a cell-averaged representation of data is presented. The original Harten's framework [13, 14, 15, 16] is here modified to allow an efficient representation of data with respect to a general weighted function. In the context of UQ, the weighted function is easily identified as the probability distribution of the input parameters.

In this paper, only the cell-average framework is analyzed and this choice allows a straightforward extension of the finite volume representation of data in the coupled physical/stochastic space as already shown in [7] employing only uniform meshes in both spaces (see later §4).

The Harten framework can be considered, as pointed out by Aràndiga and Donat in [17], as a rearrangement of the information in a set of discrete data representing different resolution levels. This rearrangement of data with the addition of a truncation procedure could yield a reduction of the computational cost and of the memory usage associated to the representation/calculation and memorization of discrete data.

The Harten framework can be viewed as a more general framework with respect to the classical wavelets framework in which the hierarchical representation of data is obtained by means of a functional basis based on a dilating equation and a so called mother wavelets. As presented in [18] the dilating equation in a general space can be difficult to solve, especially for domains of complex geometries. The Harten framework is capable to avoid the solution of a dilating equation obtaining a local polynomial basis for general geometries with, eventually, data-dependent strategies for the representation of data. All this features makes the Harten framework, an optimal starting point for the development of a general framework for the representation of data.

Two building blocks exist: a discretization operator $\mathcal{D}_k$ and a reconstruction operator $\mathcal{R}_k$. Both operators operates between the continuous space to represent (the stochastic space in this context) and one of its discrete representation, for instance the resolution level $k-$th. The knowledge of the these two operators allow to define in an unique way two other operators working on data rearrangement between different resolution levels. These discrete operators between consecutive levels k (higher resolution) and $k-1$ (lower resolution) are the operators of decimation D_k^{k-1} and prediction P_{k-1}^k.

In this paper, we consider the cell-average framework. Let us consider a function $f = f(\boldsymbol{\xi})$, $f : \Xi \subset \mathbb{R}^d \to \mathbb{R}$ with d the number of uncertain parameters. In the classical MR cell-average framework, $f \in \mathcal{F}$ where $\mathcal{F}$ is the functional space of the absolutely integrable functions $\mathcal{F} = L^1(\Xi)$. However, in the context of UQ, $\mathcal{F}$ is identified with L^2 to deal with function with finite variance. Let us consider the probability density function $p(\boldsymbol{\xi})$ and let us define the following measure:

$$\mathrm{d}\mu(\boldsymbol{\xi}) = p(\boldsymbol{\xi})\mathrm{d}\boldsymbol{\xi}. \tag{4}$$

If the stochastic space is represented by means of a non-overlapping tessellation

$$\Xi = \bigcup_{j=1}^{N_\xi} \Xi_j, \quad \text{with} \quad \Xi_i \cap \Xi_j = 0 \quad \text{if} \quad i \neq j. \tag{5}$$

the measure of each element of the tessellation can be found as follows

$$\mu(\Xi_j) = \int_{\Xi_j} \mathrm{d}\mu(\boldsymbol{\xi}). \tag{6}$$

Let us consider a set of discrete operators of discretization $\{\mathcal{D}_k\}_{k=0}^{L}$, each of them defined on a vectorial space of finite dimension

$$\mathcal{D}_k : \quad \mathcal{F} \to V_k \quad \text{with} \quad \dim(V_{k+1}) > \dim(V_k) = J_k. \tag{7}$$

The sequence $\{\mathcal{D}_k\}_{k=0}^{L}$ has to be nested according to the following properties:

- $\mathcal{D}_k$ is onto
- the null space of each level include the null space associated to the previous resolution level $\mathcal{N}(\mathcal{D}_k) \subset \mathcal{N}(\mathcal{D}_{k+1})$.

These properties reflect in the following relation between discretization operators

$$\mathcal{D}_{k+1}(f) = 0 \Rightarrow \mathcal{D}_k(f) = 0 \quad \forall f \in \mathcal{F}. \tag{8}$$

A such operator on the k-th level can be defined over the j-th cell Ξ_j^k as

$$(\mathcal{D}_k f)_j \stackrel{\text{def}}{=} \frac{1}{\mu(\Xi_j^k)} \int_{\Xi_j^k} f(\boldsymbol{\xi}) \mathrm{d}\mu(\boldsymbol{\xi}) = v_j^k. \tag{9}$$

Thanks to the onto property of each operator $\mathcal{D}_k$, the reconstruction operator $\mathcal{R}_k$ can be defined as its right-inverse

$$\mathcal{R}_k : \quad V_k \to \mathcal{F}. \tag{10}$$

The reconstruction operator is not required to be linear and this makes the Harten's multiresolution more general with respect to the wavelets framework [19].

The reconstruction operator $\mathcal{R}_k$ for the cell average setting originally has been introduced by Harten in the 1D case employing the concept of reconstruction via primitive function. In practice, the cell-averaged function is replaced by a point valued function that corresponds to its primitive in the nodes of the mesh. A more convenient approach can be adopted, following Abgrall and Sonar [20], even for multidimensional problems on unstructured meshes [16]. Fixed a polynomial degree of reconstruction r, a stencil $\mathcal{S}_j^k$ of cells with cardinality $s = s(r) = \mathrm{card}(\mathcal{S}_j^k)$ can be fixed. On each stencil $\mathcal{S}_j^k$, a polynomial $\mathcal{P}_j^k(\boldsymbol{\xi}; f)$ of degree r can be constructed. The admissibility of this stencil obeys to a Vandermonde condition (see for further details [20]). Supposing the stencils admissible, the conditions to satisfy for the computation of $\mathcal{P}_j^k$ is

$$\mathcal{D}_k(\mathcal{P}_j^k(\boldsymbol{\xi}; f))_l = \mathcal{D}_k(f)_l, \quad \forall l \in \mathcal{S}_j^k. \tag{11}$$

The reconstruction operator $\mathcal{R}_k$ in this case is exactly equal to the union of all the polynomial $\mathcal{P}_j^k$ defined on all the cells Ξ_j^k.

The two operators $\mathcal{D}_k$ and $\mathcal{R}_k$ should satisfy a consistency relationship between them

$$(\mathcal{D}_k \mathcal{R}_k)(v) = v \quad \forall v \in V_k, \tag{12}$$

thus implying $\mathcal{D}_k\mathcal{R}_k = \mathrm{I}_k$ where I_k is the identity operator on V_k.

For the nested sequence whose elements are defined in (7), the decimation operator D_k^{k-1} can be defined, which is a linear mapping between V_k onto V_{k-1}:

$$\mathrm{D}_k^{k-1}: \quad V_k \to V_{k-1}, \tag{13}$$

where

$$\mathrm{D}_k^{k-1} v^k = \mathcal{D}_{k-1} f \in V_{k-1} \quad \forall v^k = \mathcal{D}_k f \in V_k. \tag{14}$$

The decimation operator, independent from the particular f, is employed to generate recursively the set of discrete data from the highest resolution level ($k = L$) to the lowest ($k = 0$) $\{v^k\}_{k=0}^{L-1}$,

$$v^{k-1} = \mathrm{D}_k^{k-1} v^k \quad \forall k = L, L-1, \ldots, 1. \tag{15}$$

By an agglomeration (splitting) procedure, for a generic mesh, even non structured, it is always possible to obtain a less (higher) resolution level. To each cell Ξ_j^k at the lower resolution level corresponds a number of cell ($\bar{l_c}$) at the higher resolution level. To preserve the nested character between levels, the following properties between meshes should hold:

$$\Xi_j^k = \sum_l^{\bar{l_c}} \Xi_l^{k+1}. \tag{16}$$

In the following, without loss of generality, $\bar{l}_c = 2$. This happens naturally for the 1D case of equally splitted cells between levels in the case of regular nested meshes.

In this case, the decimation operator (see figure 1) could be obtained as follows

$$\begin{aligned}(\mathrm{D}_k^{k-1} v^k)_j = (\mathrm{D}_k^{k-1}\mathcal{D}_k f)_j = (\mathcal{D}_{k-1} f)_j &= \frac{1}{\mu(\Xi_j^{k-1})} \int_{\Xi_j^{k-1}} f(\boldsymbol{\xi}) \mathrm{d}\mu(\boldsymbol{\xi}) \\ &= \frac{1}{\mu(\Xi_j^{k-1})} \left(\mu(\Xi_{2j}^k)(\mathcal{D}_k f)_{2j} + \mu(\Xi_{2j-1}^k)(\mathcal{D}_k f)_{2j-1}\right).\end{aligned} \tag{17}$$

Moreover, the prediction P_{k-1}^k allows to approximate the set of data v^k from v^{k-1}

$$v^k = \mathcal{D}_k f \approx \mathcal{D}_k(\mathcal{R}_{k-1} v^{k-1}). \tag{18}$$

This leads to the definition of the prediction operator P_{k-1}^k between discrete data on successive resolution level as

$$\mathrm{P}_{k-1}^k \stackrel{\text{def}}{=} \mathcal{D}_k\mathcal{R}_{k-1}: \quad V^{k-1} \to V^k. \tag{19}$$

The prediction operator P_{k-1}^k is obtained following the definition (19) and using first the reconstruction procedure (11) for the level $k-1$th, and then applying the discretization operator $\mathcal{D}_k(\mathcal{P}_j^{k-1})$ relative to the level k.

A consistency property can be defined, $\mathrm{D}_k^{k-1}\mathrm{P}_{k-1}^k = \mathrm{I}_k$, that follows from

$$v^{k-1} = \mathrm{D}_k^{k-1} v^k = \mathrm{D}_k^{k-1}\mathcal{D}_k f = \mathrm{D}_k^{k-1}\mathcal{D}_k\mathcal{R}_{k-1} v^{k-1} = \mathrm{D}_k^{k-1}\mathrm{P}_{k-1}^k v^{k-1}. \tag{20}$$

The last element of the MR framework is constituted by the prediction error e^k

$$e^k \stackrel{\text{def}}{=} v^k - \mathrm{P}_{k-1}^k v^{k-1} = (\mathrm{I}_k - \mathrm{P}_{k-1}^k \mathrm{D}_k^{k-1}) v^k. \tag{21}$$

The prediction error satisfies (from the consistency property (20))

$$\mathrm{D}_k^{k-1} e^k = \mathrm{D}_k^{k-1}(v^k - \mathrm{P}_{k-1}^k v^{k-1}) = v^{k-1} - v^{k-1} = 0, \tag{22}$$

then it is in the null space of the decimation operator $e^k \in \mathcal{N}(\mathrm{D}_k^{k-1})$. Using the definition (13) and applying the rank theorem, it is possible to write

$$\dim(V_k) = \dim(\mathcal{N}(\mathrm{D}_k^{k-1})) + \dim(V_{k-1}) \rightarrow \dim(\mathcal{N}(\mathrm{D}_k^{k-1})) = \dim(V_k) - \dim(V_{k-1}) = J_k - J_{k-1}. \tag{23}$$

The linear independent coordinates of e^k are called wavelets or details d^k. Two operators can be defined to link the prediction error to the details, E^k and G^k, as follows

$$e^k \stackrel{\text{def}}{=} E^k d^k, \quad d^k \stackrel{\text{def}}{=} G^k e^k \quad \text{with} \quad E^k G^k : V^k \rightarrow \mathcal{N}(\mathrm{D}_k^{k-1}). \tag{24}$$

Using all the operators described in this section, a multi-resolution representation of data can be defined.

This is obtained by two procedure: the *encoding* and the *decoding*. The *encoding* moves from the highest resolution level to the lowest one applying recursively (for all $k = L, \ldots, 1$) the decimation operator and computing the details

$$\begin{cases} v^{k-1} = \mathrm{D}_k^{k-1} v^k \\ d^k = G_k(\mathrm{I}_k - \mathrm{P}_{k-1}^k \mathrm{D}_k^{k-1}) v^k. \end{cases} \tag{25}$$

The multi-resolution representation v_{MR} refers to the possibility to obtain a one-to-one correspondence between the highest resolution level v^L and the sequence of the details d^k in addition to the lowest resolution level v^0:

$$v_{\mathrm{MR}} \stackrel{\text{def}}{=} \{v^0, d^1, \ldots, d^L\}. \tag{26}$$

The *decoding* procedure is the dual procedure with respect to the *encoding*: recursively moves from the lowest resolution level v^0 together with the prediction error e^k for all the levels $k = 1, \ldots, L$

$$v^k = \mathrm{P}_{k-1}^k v^{k-1} + E_k d^k. \tag{27}$$

Ideally, *decoding* and *encoding* permit an ideal exchange of information among different resolution levels. In order to be useful, these operations are coupled with an operator of data truncation. This additive operator allows, under a certain tolerance, to eliminate the over abundant information. The compression capability opens several possibilities to the application of the multi-resolution framework to compress the data as, for instance, in the signal/image representation schemes [18] or as a fundamental brick in the solution of intrinsically multi scales problems, as demonstrated already in the first seminal works of Harten [14, 15].

The truncation is instead based on the elimination of the wavelets d^k under a prescribed tolerance. The problem statement is the following: given a sequence

of scale coefficients or wavelets for a fixed level d^k and assigned a level dependent tolerance criterion ε_k, we should generate $\hat{d}^k = \left\{\hat{d}^k_j\right\}_{j=1}^{J_k - J_{k-1}}$ according to

$$\hat{d}^k_j = \mathrm{tr}(d^k_j, \varepsilon_k) = \begin{cases} 0 & |d^k_j| \leq \varepsilon_k \\ d^k_j & \text{otherwise.} \end{cases} \tag{28}$$

Different choices exist in literature for the threshold parameter ε_k: a level independent choice $\varepsilon_k = \varepsilon$ or a dependent criterion $\varepsilon_k = \varepsilon/2^{L-k}$. Since the original work of Harten, the stability of the MR representation of the data has been studied. Harten proposed [13] to modify the *encoding* procedure in order to preserve the following condition

$$||v^L - \hat{v}^L|| \leq C\varepsilon, \tag{29}$$

with a constant C and measured in some norms as the L^1 and L^∞.

In this work, the main contribution is to adapt this framework performing the one-time encoding and truncated procedure in order to obtain a compact representation of the data in the stochastic space. This fundamental brick of the algorithm is described in the following section.

3.1 A one-time truncate and encode cell-average representation

In this section, the truncate and encode TE algorithm is described in the case of cell-average quantities. The pivotal idea of the algorithm is to identify in the prediction error e^k at a certain $k-$th level, a measure of the quality of the predictor operator P^k_{k-1}.

From classical interpolation results (see for instance [21]), note that the interpolation error diminishes, moving from a coarser level to a finer one, with respect to the local regularity of the function and to the local polynomial order of the interpolation. On the contrary, in presence of discontinuities, the error remains constant and of the order $\mathcal{O}[1]$. This means that, starting from the knowledge of a fine level k (using the discretization operators $\mathcal{D}_k$), the recursive combinations of prediction operations via the operators P^k_{k-1} and evaluations of the error e^k permits to determine the region, where the solution respects a certain accuracy criterion. In particular, if the criterion is equal to the truncation operation described above, at the end of the algorithm, the discretized set of data $\{v^k\}_{k=0}^L$ is directly related to the data $\{\hat{v}^k\}_{k=0}^L$ obtained under the same truncation criterion by the classical MR framework.

The algorithm starts with the definition of the coarsest level of resolution $k = 1$. On this level the discretization operator is applied obtaining the discrete data v^1: $v^1 = \mathcal{D}_1 f$. By decimation, it is also possible to obtain the discrete data on the level $k = 0$ knowing only v^1:

$$v^0 = \mathrm{D}^0_1 v^1. \tag{30}$$

An *encoding* step (analogous to what is normally done in the classical MR (see (25))) is then completed, by computing the linear independent coefficients d^k of e^k for $k = 1$:

$$d^k = G_k(\mathrm{I}_k - \mathrm{P}^k_{k-1}\mathrm{D}^{k-1}_k)v^k. \tag{31}$$

The truncation is applied on d^1 with respect to the threshold ε, defined by the user, and to the relation $\varepsilon_k = \varepsilon_k(\varepsilon, k)$:

$$\hat{d}^1 = \mathrm{tr}(d^1, \varepsilon_k). \tag{32}$$

This operation relies on the knowledge of the finest level ($k = L$), where the threshold is always equal to ε (see (28)). The integer $k = L$ is assigned to the finest level if the coarsest is marked as $k = 0$ and at each refinement k is increased by one.

The data d^1 are analyzed in order to locate the region of the domain, where the accuracy of the prediction, via P_{k-1}^k, is not adequate. This is accomplished in a very simple way after the truncation, by identifying the non-zero wavelets d_j^1. At each non-zero (truncated) wavelets, corresponds a region where the knowledge of the solution is not sufficient under the criterion used in the truncation (32). Then, further information are added. In particular, after the generation of the mesh on the level $k = 2$, on all the cells/points inside the regions (at level $k = 0$) used to generate the corresponding wavelets d_j^1, the discretization operator $\mathcal{D}_2$ is applied. On the contrary, in the region marked as well-described, the *decoding* procedure is performed:

$$v^2 = \mathrm{P}_1^2 v^1 + E_2 d^2 \simeq \mathrm{P}_1^2 v^1. \tag{33}$$

The assumption in the equation (33) means that for every null wavelets at a level $k-1$, the corresponding wavelets at level k are null too. In the case of non null details, the equation (33) is not applied, but substituted by a direct (exact) discretization of the function by means of the operator $\mathcal{D}_k$ for $k = 2$.

Knowing v^2 and v^1, the *encoding* is performed by computing d^2 and their truncated counterpart $\hat{d}^2$ by (28). The algorithm is then repeated until reaching the finest level L or a full satisfactory prediction, *i.e.* $d_j^k = 0$ for all $j = 1, \ldots, J_k - J_{k-1}$.

To make things clear, the algorithm is now presented in the case of 1D stochastic space. Some preliminary operation are first performed:

- Generation of a nested set of meshes $\mathcal{G}^k$ for $k = 0, \ldots, L$ (0 is the coarsest mesh):

$$\mathcal{G}^k = \left\{\Xi_j^k\right\}_{j=1}^{J_k} \quad \text{where} \quad \Xi_j^k = [\xi_{j-1}^k, \xi_j^k]. \tag{34}$$

  In this case the case of bounded probability density function is addressed and a topological tessellation for the mesh can be obtained, *i.e.* each cell has the same Lebesgue measure equal to $1/J_k$. Otherwise, in the case of unbounded pdf, the set of meshes can be built on a nested sequence of cells with the same probability measure $\mathrm{d}\mu$.

- Definition of the operator $\mathcal{D}_k$, $\mathcal{R}_k$, D_k^{k-1} and P_{k-1}^k according to §3:

$$\begin{cases} (\mathcal{D}_k f(\xi))_j = \dfrac{1}{\mu(\Xi_j^k)} \displaystyle\int_{\Xi_j^k} f(\xi) p(\xi) \mathrm{d}\xi \\ \mathcal{R}_k : (\mathcal{D}_k \mathcal{R}_k v^k)_l = (\mathcal{D}_k f(\xi))_l \quad \text{with} \quad l \in \mathcal{S}_j^k \\ (\mathrm{P}_{k-1}^k v^{k-1})_j = (\mathcal{D}_k \mathcal{R}_{k-1} v^{k-1})_j = \dfrac{1}{\mu(\Xi_j^k)} \displaystyle\int_{\Xi_j^k} \mathcal{R}_{k-1} v^{k-1} p(\xi) \mathrm{d}\xi. \end{cases} \tag{35}$$

The decimation operator can be defined when the topological relation between the cells at two different resolution levels is known. Let us consider the situation sketched in figure 1. We assume that the cells generated by the splitting of Ξ_j^{k-1}, are named as Ξ_{2j-1}^k and Ξ_{2j}^k even if this numeration does not correspond to the index j of the generating stochastic cell at the lower resolution level. The indexes numeration in figure 1 is exactly matched only if all the cells are splitted from a resolution level to the higher one. In that case, the dimensions of the spaces of the two levels $k-1$ and k are related by the following relation, $J_k/J_{k-1} = 2$. In the following, the abstract indexes $2j$ and $2j-1$ are employed to make evident the dependence of the two cells, at level k, from the generating cell Ξ_j^{k-1}. However, the indexes should always be intended in the sense described above. When a cell is split to obtain the higher resolution level (see figure 1), the measure $\mathrm{d}\mu$ is defined as follows:

$$\begin{cases} \mu(\Xi_j^{k-1}) = \mu(\Xi_{2j-1}^k) + \mu(\Xi_{2j}^k) \\ \mu(\Xi_{2j-1}^k) = \mu(\Xi_{2j}^k). \end{cases} \tag{36}$$

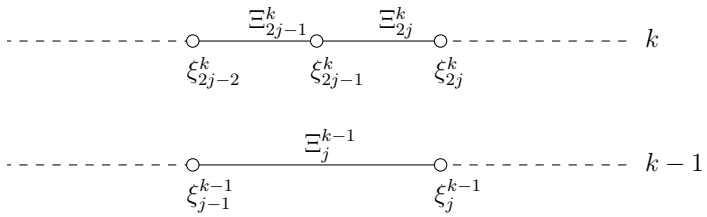

Figure 1: Example of 1D stochastic nested meshes for the cell-average setting decimation procedure.

Then, the decimation operator is simply obtained as

$$(\mathrm{D}_k^{k-1} v^k)_j = v_j^{k-1} = \frac{1}{\mu(\Xi_j^{k-1})} \left(\mu(\Xi_{2j}^k) v_{2j}^k + \mu(\Xi_{2j-1}^k) v_{2j-1}^k \right) \tag{37}$$

- Setting a proper threshold ε and a proper relation for $\varepsilon_k = \varepsilon_k(\varepsilon, k; L)$
- Discretization of the level $k = 1$: $(v^1) = (\mathcal{D}_1 f)$;
- Decimation of the discrete data v^1 to obtain $(v^0) = (\mathrm{D}_1^0 v^1)$.

The TE algorithm for cell-average setting in 1D stochastic space can be explicitly written as:

Algorithm 1: Truncate and Encode algorithm for the cell average setting in 1D stochastic space.

while $2 \leq k \leq L$ **do**
  for $j = 1, \ldots, J_{k-2}$ **do**
    Encoding: $(d^{k-1})_j = v_{2j}^{k-1} - (\mathrm{P}_{k-2}^{k-1} v^{k-2})_{2j} = v_{2j}^{k-1} - \left(\frac{1}{\mu(\Xi_{2j}^{k-1})} \int_{\Xi_{2j}^{k-1}} \mathcal{R}_{k-2} v^{k-2} p(\xi) \mathrm{d}\xi \right)$;
    Truncation: $\hat{d}_j^{k-1} = \mathrm{tr}(d_j^{k-1}, \varepsilon_{k-1})$;
  end
  for $j = 1, \ldots, J_{k-1}$ **do**
    if $\hat{d}_j^{k-1} > 0$ **then**
      Discretization: $v_{2j}^k = (\mathcal{D}_k f)_{2j} = \frac{1}{\mu(\Xi_{2j}^k)} \int_{\Xi_{2j}^k} f(\xi) p(\xi) \mathrm{d}\xi$;
      Discretization: $v_{2j-1}^k = (\mathcal{D}_k f)_{2j-1} = \frac{1}{\mu(\Xi_{2j-1}^k)} \int_{\Xi_{2j-1}^k} f(\xi) p(\xi) \mathrm{d}\xi$;
    end
  end
end

At this level, remark that the sequence of discretization operators should be nested and $\mathcal{N}(\mathcal{D}_k) \subset \mathcal{N}(\mathcal{D}_{k+1})$. This means that the error vector e^k can be represented by means of only its independent components, the wavelets d^k, thanks to the relation (24). It is always possible to write, recalling the definition of the error vector e_k (21) and the nested property of the discretization operator (17), as follows

$$\begin{aligned} e_{2j-1}^k &= v_{2j-1}^k - (\mathrm{P}_{k-1}^k v^{k-1})_{2j-1} \\ &= \frac{1}{\mu(\Xi_{2j-1}^k)} \left(\mu(\Xi_j^{k-1}) v_j^{k-1} - \mu(\Xi_{2j}^k) v_{2j}^k \right) - \frac{1}{\mu(\Xi_{2j-1}^k)} \left(\mu(\Xi_j^{k-1}) v_j^{k-1} - \mu(\Xi_{2j}^k) (\mathrm{P}_{k-1}^k v^{k-1})_{2j} \right) \\ &= \frac{\mu(\Xi_{2j}^k)}{\mu(\Xi_{2j-1}^k)} \left(\mathrm{P}_{k-1}^k v^{k-1})_{2j} - v_{2j}^k \right) = -\frac{\mu(\Xi_{2j}^k)}{\mu(\Xi_{2j-1}^k)} d_j^k. \end{aligned} \tag{38}$$

The first loop should be performed in order to compute all the *wavelets* d_j^k, while the second loop is performed over the whole set of cells belonging to the resolution level. In particular, the error vector component is compared with the threshold for deciding whether the discretization via the model evaluation is necessary. In the second loop, in the case of a nested sequence, with splitting based on the probability measure, the local error is equal to *wavelet* computed over the same cell Ξ_j^{k-1} (see equation (38)). Therefore, the truncated wavelet is exactly equal to the truncated component of the error.

In the classical framework, the first step is the *encoding* procedure moving from the finest level to the coarsest. In this case, the explicit evaluation of the function f is performed at the finest level while the other levels are obtained by agglomeration. In the present paper, the encoding is performed proceeding from the coarsest level. Each time a higher resolution level is added, *i.e* k, the function is explicitly evaluated via the discretization operator $\mathcal{D}_k$. Due to numerical errors, the relation (14) could not hold. In such a case, the wavelets d^k are not the linear independent components of

the error vector e^k. For representing the error vector in terms of its independent components d^k, the Discetrize Agglomerate Decimate (DAD) algorithm is introduced. The DAD algorithm consists in the following operations

Algorithm 2: DAD algorithm.

Discretization:

$$v^k_{2j} = \frac{1}{\mu(\Xi^k_{2j})} \int_{\Xi^k_{2j}} f(\xi)p(\xi)\mathrm{d}\xi \ ;$$

$$v^k_{2j-1} = \frac{1}{\mu(\Xi^k_{2j-1})} \int_{\Xi^k_{2j-1}} f(\xi)p(\xi)\mathrm{d}\xi \ ;$$

Agglomeration:

$$\mu(\Xi^{k-1}_j) = \mu(\Xi^k_{2j-1}) + \mu(\Xi^k_{2j}) \ ;$$

Decimation:

$$(\mathrm{D}^{k-1}_k v^k)_j = v^{k-1}_j = \frac{1}{\mu(\Xi^{k-1}_j)} \left(\mu(\Xi^k_{2j})v^k_{2j} + \mu(\Xi^k_{2j-1})v^k_{2j-1}\right)$$

The DAD algorithm should be always performed before the *Encoding* in the TE algorithm 2. The introduction of the DAD algorithm is a peculiarity of the cell-average framework, while the point-value setting does not require any similar procedure because two successive levels are constituted by a set of points in the intersection of the two spaces.

Another peculiarity of the cell average framework is the presence of integral quantities that requires different evaluation in each cell, according to the numerical rule used to obtain the integrals in the discretization operator (9). The family of Newton-Cotes formula, employing only equally spaced points, is the best choice in term of computational cost; this family of quadrature rule is both nested and based on equally spaced points. The three point quadrature rule of Newton Cotes, known also as the Cavalieri-Simpson rule, is employed in this work:

$$\int_a^b f(\xi)\mathrm{d}\mu(\xi) \approx \frac{b-a}{6}\left(f(a) + 4f\left(\frac{a+b}{2}\right) + f(b)\right). \tag{39}$$

When a cell is split, it is easy to see that only three of the six points required (three for each cells) should be computed again. On the contrary, the points employed at the previous level can be re-employed thanks to the nested nature of the meshes. This makes the sequence of cell evaluations from the coarsest resolution level to the finest one, only a hierarchical representation without extra computational effort. For instance, if a Gauss (two points) quadrature rule would be employed, the point of a previous level could not be used for the evaluation, of the integrals, at successive resolution levels. This feature is a key aspect when the MR framework is coupled (see section §5) with the semi-intrusive scheme presented in the following section.

3.2 ENO polynomial reconstruction for the MR setting

In this section, further details on the polynomial interpolation are provided. The $\mathcal{R}_k$ operator, from a practical point of view, can be obtained by the union of all the polynomial obtained by the conservative interpolation techniques described by the equation (11). Two different operations are relative to the piecewise polynomial approximation $\mathcal{P}_j$. The first is to obtain $\mathcal{P}^k_j$ from the mesh at the resolution level k and, of course, from the cell average quantities at this resolution level. The second operation is the prediction of a cell average value (for a cell entirely contained in the support of the polynomial $\mathcal{P}^k_j$) at the successive resolution level (see equation (19)). To make things clearer, the case of uniform

probability distribution is here addressed. The first task is to define the polynomial representation for a second order polynomial piecewise approximations ($r = 2$), over the stochastic cell Ξ_j:

$$\mathcal{P}_j = a(\xi - \xi_j)^2 + b(\xi - \xi_j) + c, \tag{40}$$

where ξ_j is the coordinate of the center of the stochastic cell.

To obtain the coefficients a, b and c, the conditions (11) must be fulfilled for a certain stencil. In the case of centered reconstruction, the stencil is fixed and equal to $\mathcal{S}_j = \{\Xi_{j-1}, \Xi_j, \Xi_{j+1}\}$. A linear system can be obtained as

$$\begin{cases} \mathbb{E}(\mathcal{P}_j^k \,|\, \Xi_{j-1}) = \dfrac{1}{\mu(\Xi_{j-1}^k)} \displaystyle\int_{\Xi_{j-1}^k} \mathcal{P}_j^k \mathrm{d}\xi = \mu(\Xi_{j-1}^k) v_{j-1}^k \\ \mathbb{E}(\mathcal{P}_j^k \,|\, \Xi_j) = \dfrac{1}{\mu(\Xi_j^k)} \displaystyle\int_{\Xi_j^k} \mathcal{P}_j^k \mathrm{d}\xi = \mu(\Xi_j^k) v_j^k \\ \mathbb{E}(\mathcal{P}_j^k \,|\, \Xi_{j+1}) = \dfrac{1}{\mu(\Xi_{j+1}^k)} \displaystyle\int_{\Xi_{j+1}^k} \mathcal{P}_j^k \mathrm{d}\xi = \mu(\Xi_{j+1}^k) v_{j+1}^k, \end{cases} \tag{41}$$

where the linear operator $\mathbb{E}(\bullet \,|\, \Xi)$ becomes (on the generic cell Ξ_j)

$$\mathbb{E}(\mathcal{P}_j^k \,|\, \Xi_j) = a\, \mathbb{E}((\xi - \xi_j)^2 \,|\, \Xi_j) + b\, \mathbb{E}((\xi - \xi_j) \,|\, \Xi_j) + c. \tag{42}$$

If the integration is performed analytically, with respect to the parameter $(\xi - \xi_j)$, the system becomes

$$\begin{pmatrix} \mathbb{E}((\xi-\xi_j)^2 \,|\, \Xi_{j-1}) & \mathbb{E}((\xi-\xi_j) \,|\, \Xi_{j-1}) & 1 \\ \mathbb{E}((\xi-\xi_j)^2 \,|\, \Xi_j) & \mathbb{E}((\xi-\xi_j) \,|\, \Xi_j) & 1 \\ \mathbb{E}((\xi-\xi_j)^2 \,|\, \Xi_{j+1}) & \mathbb{E}((\xi-\xi_j) \,|\, \Xi_{j+1}) & 1 \end{pmatrix} \begin{pmatrix} a \\ b \\ c \end{pmatrix} = A(\xi - \xi_j) \begin{pmatrix} a \\ b \\ c \end{pmatrix} = \begin{pmatrix} \mu(\Xi_{j-1}^k) v_{j-1}^k \\ \mu(\Xi_j^k) v_j^k \\ \mu(\Xi_{j+1}^k) v_{j+1}^k \end{pmatrix}, \tag{43}$$

where the matrix $A = A(\xi - \xi_j)$ is dependent from the stochastic cell Ξ_j via its coordinate ξ_j. From a practical point of view, when the polynomial reconstruction should be performed over a cell Ξ_j, the matrix $A^{-1}(\xi - \xi_j)$ is first evaluated and then the vector of coefficients is obtained by the matrix vector product with the right hand side that depends from both the resolution level k and the stencil $\mathcal{S}_j$.

However, the procedure described above should be modified if the ENO interpolation is required. The only modification concerns the choice of the stencil: the procedure select the less oscillatory one between the following $\{\Xi_{j-2}, \Xi_{j-1}, \Xi_j\}$, $\{\Xi_{j-1}, \Xi_j, \Xi_{j+1}\}$ and $\{\Xi_j, \Xi_{j+1}, \Xi_{j+2}\}$. The smoothest one is selected choosing the one with $\min(|a|)$ following [22]. Obviously, at the boundaries of the domain, the stencil is always modified to be inside the domain. This is a key aspect if the higher accuracy is desired. With the modification of the stencil, the scheme preserves its maximal accuracy as it is shown for the solution of the stochastic linear advection equation with smooth solution in §6.1.

The second task to solve is the prediction of a cell average v_j^{k+1} at the next following resolution level, if the polynomial $\mathcal{P}_j^k$ reconstruction at the previous resolution level is available (the cell $\Xi_j^{k+1} \subset \Xi_j^k$ as required by the nested character of the discretization procedure). This task is accomplished analytically in

the following way. The expectancy operator is applied to the polynomial $\mathcal{P}_j^k$ over the stochastic cell $\Xi_j^{k+1} \subset \Xi_j^k$

$$\mathbb{E}(\mathcal{P}_j^k \,|\, \Xi_j^{k+1}) = a\,\mathbb{E}((\xi - \xi_j^k)^2 \,|\, \Xi_j^{k+1}) + b\,\mathbb{E}((\xi - \xi_j^k) \,|\, \Xi_j^{k+1}) + c, \qquad (44)$$

where the terms $\mathbb{E}((\xi-\xi_j^k)^2 \,|\, \Xi_j^{k+1})$ and $\mathbb{E}((\xi-\xi_j^k) \,|\, \Xi_j^{k+1})+c)$ can be analytically evaluated when the cell Ξ_j^{k+1} is defined.

The procedure described in this section is used in SI scheme in order to obtain the polynomial representation of the functions along the stochastic space to evaluate the expectancy of the flux function.

4 The semi-intrusive finite volume formulation for pde

In this section, the semi-intrusive (SI) method of Abgrall and Congedo is sketched. The interested reader can refer to [7] for a complete presentation of the numerical scheme and its application to different test cases.

The SI method is an intrusive scheme for the propagation of uncertainties, that requires only a limited number of modification to an existing numerical code. In particular, the SI scheme relies on the deterministic formulation available in a numerical code. Moreover, the number of equations remains equal to the original deterministic formulation, not as in the intrusive polynomial chaos method (see [5]). This feature permits to obtain intrusive stochastic formulation even for high order schemes. In the present work, a second order MUSCL-Hancock method (MHM) is employed to formulate the deterministic part of the scheme. This result, to the best of our knowledge, is the first adaptive intrusive scheme of high-order. Another adaptive intrusive strategy based on data-independent wavelets limited only to first order in time and space is the work of Tryoen et al. [11]. This work is the first to introduce wavelets adaptivity into an intrusive stochastic formulation by means of the polynomial chaos technique, but remain very limited in its generality requiring for each case *ad hoc* modifications.

4.1 MUSCL-Hancock deterministic numerical formulation

The MHM is a slightly different approach with respect to the classical predictor-corrector MUSCL approach. It requires only the computation of slopes in the predictor step. Moreover, it does not require the solution of Riemann problems in the predictor step. The corrector step is based on the evolution of cell-average quantities, taking into account their contribution related to the flux at interfaces obtained by the solution of a Riemann problem. Let us consider a 1D scalar conservation law

$$\frac{\partial u(x,t)}{\partial t} + \frac{\partial f(u(x,t))}{\partial x} = 0, \qquad (45)$$

where $x \in \Omega \subset \mathbb{R}$ is the physical space and $t \in T \subset \mathbb{R}^+$ is the time space. The physical space is divided in a set of non-overlapping cells $\mathcal{C}_i$ with $\Omega = \bigcup_i \mathcal{C}_i$. The classical first order Godunov scheme, applied to (45), is obtained introducing the so-called cell-average $\bar{u}_i$ on each cell $\mathcal{C}_i$:

$$\bar{u}_i(t) = \frac{1}{|\mathcal{C}_i|}\int_{\mathcal{C}_i} u(x,t)\mathrm{d}x, \qquad (46)$$

where $|\mathcal{C}_i|$ indicates the volume of the cell. Van Leer [23, 24] proposed to consider non-constant data on each cell to achieve a higher accuracy in the so-called Monotone Upstream-centred Scheme for Conservation Laws (MUSCL). The piecewise linear approximation is used for the solution $u(x,t)$ on the cell $|\mathcal{C}_i|$:

$$u(x,t_n) = \bar{u}_i^n + \sigma_i^n (x - x_i) \quad \text{with} \quad x_{i_L} \leq x \leq x_{i_R}, \tag{47}$$

with σ_i^n the so-called slope. Of course, the choice of $\sigma_i^n = 0$ leads to the Godunov scheme. A slope limiter should be introduced near the discontinuity to avoid oscillations. In this work, both the Roe's superbee limiter and the van Leer limiters are employed. The superbee limiter in its limited slope form is

$$\begin{cases} \sigma_i^n = \text{maxmod}\left(\sigma_{(1)}^n, \sigma_{(2)}^n\right) \\ \sigma_{(1)}^n = \text{minmod}\left(\left(\dfrac{\bar{u}_{i+1}^n - \bar{u}_i^n}{|\mathcal{C}_i|}\right), 2\left(\dfrac{\bar{u}_i^n - \bar{u}_{i-1}^n}{|\mathcal{C}_i|}\right)\right) \\ \sigma_{(2)}^n = \text{minmod}\left(2\left(\dfrac{\bar{u}_{i+1}^n - \bar{u}_i^n}{|\mathcal{C}_i|}\right), \left(\dfrac{\bar{u}_i^n - \bar{u}_{i-1}^n}{|\mathcal{C}_i|}\right)\right), \end{cases} \tag{48}$$

where the minmod and maxmod functions are defined as follows

$$\text{minmod}(a,b) = \begin{cases} a & \text{if} \quad |a| < |b| \quad \text{and} \quad ab > 0 \\ b & \text{if} \quad |a| > |b| \quad \text{and} \quad ab > 0 \\ 0 & \text{if} \quad ab <= 0 \end{cases}$$

$$\text{maxmod}(a,b) = \begin{cases} a & \text{if} \quad |a| > |b| \quad \text{and} \quad ab > 0 \\ b & \text{if} \quad |a| < |b| \quad \text{and} \quad ab > 0 \\ 0 & \text{if} \quad ab <= 0. \end{cases}$$

The van Leer limiter, in the form of slope limiter, is defined as (see Toro [24] for further details)

$$\sigma_i^n = \begin{cases} \text{MIN}\left(\dfrac{2R}{1+R}, \dfrac{2}{1+R}\right) \dfrac{\bar{u}_{i+1}^n - \bar{u}_{i-1}^n}{2\Delta x} & \text{if} \quad R > 0 \\ 0 & \text{if} \quad R \leq 0, \end{cases} \tag{49}$$

where R is the ratio between successive slopes $R = (\bar{u}_i^n - \bar{u}_{i-1}^n)/(\bar{u}_{i+1}^n - \bar{u}_i^n)$.

The MHM is then introduced in order to avoid the problem related to the solution of the so-called generalized Riemann problem, in which the two states are not constant. The fully discrete second order MHM, for computing the cell averaged solution $\bar{u}_i^{n+1}$, consists of the following three steps:

- Step 1 - For each cell $\mathcal{C}_\ell \in \{\mathcal{C}_{i-1}, \mathcal{C}_i, \mathcal{C}_{i+1}\}$, the solution at the interface is computed according to

$$\begin{cases} u_{\ell_L}^n = \bar{u}_\ell^n - \sigma_\ell^n \dfrac{|\mathcal{C}_\ell|}{2} \\ u_{\ell_R}^n = \bar{u}_\ell^n + \sigma_\ell^n \dfrac{|\mathcal{C}_\ell|}{2} \end{cases} \tag{50}$$

- Step 2 - On each cell $\mathcal{C}_\ell \in \{\mathcal{C}_{i-1}, \mathcal{C}_i, \mathcal{C}_{i+1}\}$, the solution evolved of a half time step employing the flux function $f = f(u)$:

$$\begin{cases} u^{\Uparrow}_{\ell_R} = \bar{u}_{\ell_R} + \dfrac{1}{2}\dfrac{\Delta t}{|\mathcal{C}_\ell|}\left(f(u^n_{\ell_L}) - f(u^n_{\ell_R})\right) \\ u^{\Uparrow}_{\ell_L} = \bar{u}_{\ell_L} + \dfrac{1}{2}\dfrac{\Delta t}{|\mathcal{C}_\ell|}\left(f(u^n_{\ell_L}) - f(u^n_{\ell_R})\right) \end{cases} \tag{51}$$

- Step 3 - The cell-averaged value on the cell $\mathcal{C}_i$ evolves following

$$\bar{u}_i^{n+1} = \bar{u}_i^n - \frac{\Delta t}{|\mathcal{C}_i|}\left(\mathcal{F}^{\mathrm{RM}}\left(u^{\Uparrow}_{i-1_R}, u^{\Uparrow}_{i_L}\right) - \mathcal{F}^{\mathrm{RM}}\left(u^{\Uparrow}_{i_R}, u^{\Uparrow}_{i+1_L}\right)\right). \tag{52}$$

The symbol $\mathcal{F}^{\mathrm{RM}}$ is employed to indicate the flux evaluated at the interface, after the solution of the Riemann problem defined by two constant states based on the evolved extrapolated values. For the linear advection §6.1 and Burgers equation §6.2, an exact Riemann solver is used. Moreover, in the case of the Euler system of equations §6.3, the Roe-Pike method is employed with the Harten-Hyman entropy fix following [24].

The time advancing formula is then limited to a stencil of only three cells $\mathcal{C}_{i-1}$, $\mathcal{C}_i$ and $\mathcal{C}_{i+1}$ but the computation of the slopes for the cells $\mathcal{C}_{i-1}$ and $\mathcal{C}_{i+1}$ requires (see (48) and (49)) also to know the solution on the two sourrounding cells $\mathcal{C}_{i-2}$ and $\mathcal{C}_{i+2}$. The average solution $\bar{u}_i^{n+1}$, on each cell $\mathcal{C}_i$ at time $t_{n+1} = t_n + \Delta t$, can be computed knowing the solution on the augmented stencil $\left\{\bar{u}^n_{i-2}, \bar{u}^n_{i-1}, \bar{u}^n_i, \bar{u}^n_{i+1}, \bar{u}^n_{i+2}\right\}$. In the following, the notation $\bar{u}_i^{n+1} = \mathrm{MHM}\left(\bar{u}^n_{i-2}, \bar{u}^n_{i-1}, \bar{u}^n_i, \bar{u}^n_{i+1}, \bar{u}^n_{i+2}, \Delta t\right)$ is used to identify the ensemble of the operation described above. The aim is to evaluate the updated value in time of a certain cell $\bar{u}_i^{n+1}$, knowing the solution at the previous time step.

4.2 Semi-intrusive formulation for the MHM

The SI version of the MHM (here presented in the 1D stochastic case without loss of generality) can be obtained adding one dimension more (the stochastic space) with a finite-volume like representation. In particular, the conditional expectancy operator, defined on the stochastic cell Ξ_j, is introduced according to the following definition:

$$\mathbb{E}(\bullet \,|\, \Xi_j) = \frac{1}{\mu(\Xi_j)} \int_{\Xi_j} \bullet(x, \xi, t)\, p(\xi, t)\, \mathrm{d}\xi. \tag{53}$$

If the conditional expectancy operator is applied to the step three of the MHM scheme (52), the following scheme is obtained:

$$\mathbb{E}(u_i^{n+1} \,|\, \Xi_j) = \mathbb{E}(u_i^n \,|\, \Xi_j) - \frac{\Delta t}{|\mathcal{C}_i|}\left(\mathbb{E}(\mathcal{F}^{\mathrm{RM}}\left(u^{\Uparrow}_{i-1_R}, u^{\Uparrow}_{i_L}\right) \,|\, \Xi_j) - \mathbb{E}(\mathcal{F}^{\mathrm{RM}}\left(u^{\Uparrow}_{i_R}, u^{\Uparrow}_{i+1_L}\right) \,|\, \Xi_j)\right). \tag{54}$$

The evaluation of the updated conditional expectancy value on the cell Ξ_j, is obtained by evaluating the conditional expectancy contribution related to the numerical fluxes $\mathbb{E}(\mathcal{F}^{\mathrm{RM}}\left(u^{\Uparrow}_{i-1_R}, u^{\Uparrow}_{i_L}\right) \,|\, \Xi_j)$ and $\mathbb{E}(\mathcal{F}^{\mathrm{RM}}\left(u^{\Uparrow}_{i_R}, u^{\Uparrow}_{i+1_L}\right) \,|\, \Xi_j)$. To evaluate this integral contribution, a polynomial representation of the physical

averaged solution with respect to the stochastic dimensions, has to be obtained. The conservative interpolation procedure, already presented in §3 to obtain the reconstruction operator $\mathcal{R}_k$, can be adopted requiring for the polynomial $\mathcal{P}_j(\xi)$:

$$\mathbb{E}(P_\ell(\xi)\,|\,\Xi_\ell) = \mathbb{E}(u\,|\,\Xi_\ell) \quad \forall \Xi_\ell \in \mathcal{S}_j \tag{55}$$

If the stencil $\mathcal{S}_j$ is chosen with a cardinality $s = s(r) = \mathrm{card}(\mathcal{S}_j) = r+1$ (for a 1D space), a polynomial $\mathcal{P}_j(\xi)$ of degree r can be built.

The polynomial representation $\mathcal{P}_j(\xi)$ can be injected into the steps 1 (50) and 2 (51) of the MHM. If the Cavalieri-Simpson rule (using three quadrature points $ng = 3$) is adopted for the quadrature, the SI scheme for the MHM can be recasted in a form that makes easy the use of MR stochastic representation of data.

We assume a uniform tessellation for the physical and stochastic space, with a number of cells equal to N_x and N_ξ, respectively and a constant time step Δt. The first step is to evaluate the initial condition in terms of conditional expectancies. This can be obtained easily via a tensorization of the quadrature rule and evaluating the analytical value of the function $u(x,\xi,0)$. This step yields the stochastic initial condition $\mathbb{E}(u_i(x,\xi,0)\,|\,\Xi_j)$ for all $i = 1,\dots,N_x$ and $j = 1,\dots,N_\xi$.

The SI algorithm becomes:

Algorithm 3: Semi-intrusive version of the MUSCL-Hancock method for a 1D stochastic space.

for $n = 1,\dots,N_t$ **do**
  for $i = 1,\dots,N_x$ **do**
    for $j = 1,\dots,N_\xi$ **do**
      Polynomial reconstruction (via (55)) over $\Xi_j = [\xi_{j-1},\xi_j]$
      $\Rightarrow \mathcal{P}_j(\xi)$;
      for $ng = 1,\dots,3$ **do**
        $\xi_{ng} = \xi_{j-1} + \frac{\xi_j - \xi_{j-1}}{2}(ng-1)$;
        Step 1 (see (50))
        $\Rightarrow \forall \mathcal{C}_\ell \in \{\mathcal{C}_{i-1},\mathcal{C}_i,\mathcal{C}_{i+1},\} \rightarrow \left\{u^n_{\ell_L}(\xi_{ng}), u^n_{\ell_R}(\xi_{ng})\right\}$;
        Step 2 (see (51))
        $\Rightarrow \forall \mathcal{C}_\ell \in \{\mathcal{C}_{i-1},\mathcal{C}_i,\mathcal{C}_{i+1},\} \rightarrow \left\{u^{\Uparrow}_{\ell_L}(\xi_{ng}), u^{\Uparrow}_{\ell_R}(\xi_{ng})\right\}$;
      end
      Flux expectancy computation:
      $\mathbb{E}(\mathcal{F}^{\mathrm{RM}}_L\,|\,\Xi_j) = \sum_{ng=1}^{3} w_{ng}\ \mathcal{F}^{\mathrm{RM}}\left(u^{\Uparrow}_{i-1_R}(\xi_{ng}), u^{\Uparrow}_{i_L}(\xi_{ng}), \xi_{ng}\right)$;
      $\mathbb{E}(\mathcal{F}^{\mathrm{RM}}_R\,|\,\Xi_j) = \sum_{ng=1}^{3} w_{ng}\ \mathcal{F}^{\mathrm{RM}}\left(u^{\Uparrow}_{i_R}(\xi_{ng}), u^{\Uparrow}_{i+1_L}(\xi_{ng}), \xi_{ng}\right)$;
      Time update:
      $\mathbb{E}(\bar{u}^{n+1}_i\,|\,\Xi_j) = \mathbb{E}(\bar{u}^{n}_i\,|\,\Xi_j) - \frac{\Delta t}{|\mathcal{C}_i|}\left(\mathbb{E}(\mathcal{F}^{\mathrm{RM}}_L\,|\,\Xi_j) - \mathbb{E}(\mathcal{F}^{\mathrm{RM}}_R\,|\,\Xi_j)\right)$
    end
  end
end

where $\mathbb{E}(\mathcal{F}^{\mathrm{RM}}_L\,|\,\Xi_j) = \mathbb{E}(\mathcal{F}^{\mathrm{RM}}\left(u^{\Uparrow}_{i-1_R}, u^{\Uparrow}_{i_L}\right)\,|\,\Xi_j)$ and $\mathbb{E}(\mathcal{F}^{\mathrm{RM}}_R\,|\,\Xi_j) = \mathbb{E}(\mathcal{F}^{\mathrm{RM}}\left(u^{\Uparrow}_{i_R}, u^{\Uparrow}_{i+1_L}\right)\,|\,\Xi_j)$.

5 The overall multiresolution adaptive-SI scheme

In the previous section, the SI scheme applied to the MHM is presented. In this section, the adaptive version of the numerical algorithm (aSI) is described. The main difference, referring to the algorithm 3 is in the internal loop, on j, concerning the stochastic cells. This loop should be substituted by the application of the TE algorithm 1. The discretization step is performed by the application of the MHM, as presented in the internal loop (on j), in the algorithm 3. The complete aSI scheme is:

Algorithm 4: Semi-intrusive version of the MUSCL-Hancock method for a 1D stochastic space.

for $n = 1, \dots, N_t$ **do**
  for $i = 1, \dots, N_x$ **do**
    while $2 \leq k \leq L$ **do**
      for $j = 1, \dots, J_{k-2}$ **do**
        Encoding: $d_j^{k-1} = v_{2j}^{k-1} - (\mathrm{P}_{k-2}^{k-1} v^{k-2})_{2j} = v_{2j}^{k-1} - \left(\frac{1}{\mu(\Xi_{2j}^{k-1})} \int_{\Xi_{2j}^{k-1}} \mathcal{R}_{k-2} v^{k-2} p(\xi) \mathrm{d}\xi \right)$;
        Truncation: $\hat{d}_j^{k-1} = \mathrm{tr}(d_j^{k-1}, \varepsilon_{k-1})$;
      end
      for $j = 1, \dots, J_{k-1}$ **do**
        if $\hat{d}_j^{k-1} > 0$ **then**
          Discretization:
          for $\Xi_q \in \left\{ \Xi_{2j-1}^k, \Xi_{2j}^k \right\}$ **do**
            for $ng = 1, \dots, 3$ **do**
              Polynomial evaluation:
              $\bar{u}(x, \xi_{ng}, t_n) \simeq (\mathcal{D}_k \mathcal{R}_L v^L(t_n))(\xi_{ng})$
              Step 1 (see (50)) $\Rightarrow \forall \mathcal{C}_\ell \in \{\mathcal{C}_{i-1}, \mathcal{C}_i, \mathcal{C}_{i+1},\} \rightarrow \left\{ u_{\ell_L}^n(\xi_{ng}), u_{\ell_R}^n(\xi_{ng}) \right\}$
              Step 2 (see (51)) $\Rightarrow \forall \mathcal{C}_\ell \in \{\mathcal{C}_{i-1}, \mathcal{C}_i, \mathcal{C}_{i+1},\} \rightarrow \left\{ u_{\ell_L}^{\Uparrow}(\xi_{ng}), u_{\ell_R}^{\Uparrow}(\xi_{ng}) \right\}$
            end
            Flux expectancy computation:
            $\mathbb{E}(\mathcal{F}_L^{\mathrm{RM}} \,|\, \Xi_q) = \sum_{ng=1}^{3} w_{ng} \, \mathcal{F}^{\mathrm{RM}} \left(u_{i-1_R}^{\Uparrow}(\xi_{ng}), u_{i_L}^{\Uparrow}(\xi_{ng}), \xi_{ng} \right)$
            $\mathbb{E}(\mathcal{F}_R^{\mathrm{RM}} \,|\, \Xi_q) = \sum_{ng=1}^{3} w_{ng} \, \mathcal{F}^{\mathrm{RM}} \left(u_{i_R}^{\Uparrow}(\xi_{ng}), u_{i+1_L}^{\Uparrow}(\xi_{ng}), \xi_{ng} \right)$
            Cell agglomeration of $\mathbb{E}(u_i^n \,|\, \Xi_q)$ via equation (56)
            Time update:
            $\mathbb{E}(\bar{u}_i^{n+1} \,|\, \Xi_q) = \mathbb{E}(\bar{u}_i^n \,|\, \Xi_q) - \frac{\Delta t}{|\mathcal{C}_i|} \left(\mathbb{E}(\mathcal{F}_L^{\mathrm{RM}} \,|\, \Xi_q) - \mathbb{E}(\mathcal{F}_R^{\mathrm{RM}} \,|\, \Xi_q) \right)$
          end
        end
      end
    end
    Reconstruction: $(\mathcal{D}_L \mathcal{R}_L v^L)_l = (\mathcal{D}_L \bar{u}(x_i, \xi, t_{n+1}))_l \quad \text{with} \quad l \in \mathcal{S}_j^L$;
  end
end

The reconstruction operator $\mathcal{R}_k$ for each cell Ξ_j is the polynomial $\mathcal{P}_j$ reconstructed for the SI scheme. A link between the MR representation and the SI scheme exists since the polynomial representation of the data in the stochastic space is the same for the SI and TE. The polynomial reconstruction is carried

out when the algorithm attain the highest resolution level (indicated in the algorithm by $k = L$) and the reconstruction operator $\mathcal{R}_L$ is then obtained and stored. The reconstruction operator is then used, for the polynomial evaluation before Step 1. The physical cell-averaged values are obtained, for each quadrature points ξ_{ng}, applying the discretization operator $\mathcal{D}_k$. Moreover, a conservative interpolation is also present into the MR algorithm, where the operator $\mathcal{R}_k$ is used to obtain the wavelets during the *encoding* procedure.

One important feature of the aSI algorithm is the possibility to locally refine/derefine the stochastic space, as a function of the variation of the solution during the computation. At the end of each time step, for each physical location, the algorithm produces a sequence of conditional expectancies $\mathbb{E}(u^n \,|\, \Xi_j)$ with different measures $\mu(\Xi_j)$, due to the local refinement/derefinement of the tessellation. The TE strategy starts from the coarsest level to the finest (until some cell have to be split or the maximum resolution level is reached). In practice, if a cell has not to be splitted, it is moved at the highest resolution level. The local variation of the cell measure yields a strong relation between the actual level of evaluation of the scheme, and the maximum level (locally) reached at the previous time step (and consequently the measure of each cell). Two problems exist: the agglomeration of a cell at a time n, and the splitting of a cell at a time $n+1$. The MR framework presented is based on a nested subdivision of the cell. Then, at the end of the TE algorithm, each cell belonging to the coarsest level $k = 0$, will result in a set of cells. When the TE algorithm requires the application of the SI-MHM at a generic level k, an equivalent conditional expectancy $\mathbb{E}(u \,|\, \Xi_j^k)$ evaluated at time n is computed by applying the equation (54). This conditional expectancy should be obtained by the agglomeration of all the stochastic cells belonging to Ξ_j^k at time n, following the exact definition:

$$\mathbb{E}(u \,|\, \Xi_j^k) = \frac{1}{\mu(\Xi_j^k)} \sum_{\Xi_\ell \subseteq \Xi_j^k} \mu(\Xi_\ell) \mathbb{E}(u \,|\, \Xi_\ell). \tag{56}$$

Obviously, it is easy to verify that the limit case is the one with a cell not subdivided, then the equation (56) reduces to an identity. Due to the nested sequences of operators and meshes, a cell would be always constituted by an integer number of cells at the end of the TE algorithm (see algorithm 1). A sketch of a possible situation for the agglomeration of a cell Ξ_j^k is reported in figure 2.

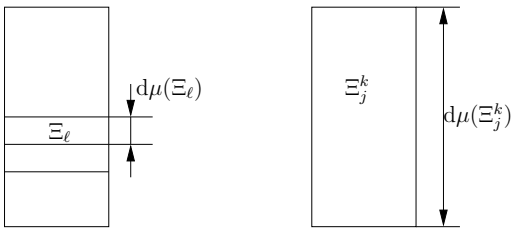

Figure 2: Example of the agglomeration procedure to obtain a coarser cell Ξ_j even if the TE algorithm yields a set of children cells.

The other issue is related to reduce the computational cost basing on the computed quantities, when a cell has to be split. For this reason, the quadrature

rule of Newton-Cotes is adopted. In this case, the entire set of degrees of freedom (dof) can be saved, if the cell has to be split. Let us consider the figure 3, where the Cavalieri-Simpson rule is used. On the left, the cell at level k is represented with its dof, the circles are used for the value of $\bar{u}_i$ obtained via the polynomial $\mathcal{P}_j$ (the polynomial evaluation step in the algorithm 4), and squares for the fluxes obtained after the application of the step 1 and 2 of the MHM. When the cell is split in two cells, only three points have to be added (the numerical scheme has to be applied). On the contrary, the other points can be obtained directly from the mother cell at level k. In the figure 3, the black circle/squares represent the new points to compute. In practice, the black points are associated to the values for $\bar{u}_i$ obtained by interpolation and the fluxes are obtained via the Step 1 and 2; otherwise, they are only recovered from the mother cell. Finally, the fluxes conditional expectancy computation is performed easily combining the new fluxes (black) and the old ones (white) with the correct weights for the quadrature.

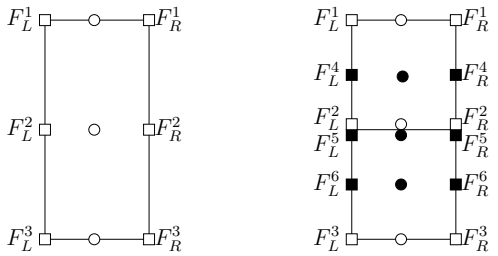

Figure 3: Example of a splitting procedure to save the computational cost associated to the degree of freedom already computed. On the left the cell at level of resolution k is reported while on the right the corresponding split cells are reported with the new points to explicitly add (black symbols).

The nested procedure described above allows to extend the accuracy of the quadrature rule even to high-order Newton-Cotes formula. Moreover, in the present work, the three points Cavalieri-Simpson rule (see (39)) is employed. The error is proportional to the fourth derivative of the integrand, so the rule is fully accurate to polynomial function of order equal or less than three (see [21] for further details). In the following, the variance of the outputs of interest is computed. In this case, the quadrature of the polynomial $\mathcal{P}_j$ squared has to be evaluated on each cell $\Xi_j = [\xi_a, \xi_b]$. In order to attain the exact integration of $\mathcal{P}_j^2$, the closed four points Newton-Cotes rule (also known as the Boole's rule) is employed

$$\int_{\Xi_j} f(\xi)\mathrm{d}\xi = \frac{\xi_b - \xi_a}{90}\left(7f(\xi_a) + 32f\left(\xi_a + \frac{\xi_b - \xi_a}{4}\right) + 12f\left(\xi_a + \frac{\xi_b - \xi_a}{2}\right) + 32f\left(\xi_a + 3\frac{\xi_b - \xi_a}{4}\right) + 7f(\xi_b)\right). \tag{57}$$

The last five points rule has an error $\mathcal{O}(f^{(6)}(\eta))$, where $\eta \in]\xi_a, \xi_b[$, so it is able to integrate exactly polynomial function of order equal to five.

6 Numerical results

In this section, the aSI scheme derived in §5 is applied to a set of test problems. The aim is to show the convergence properties and to provide some evidence of the advantage to employ an adaptive representation of the solution in the stochastic space. For all the problems, the expectancy and the variance of the some outputs are computed according to the definitions (3) with respect to their exact value. Different 1D-1D test cases are taken into account. The linear advection problem is solved for both smooth and discontinuous initial conditions in section §6.1. In the first case, the uncertainty is considered in the initial condition, while in the discontinuous case an uncertain advection velocity is considered. For this test case, both the convergence curves for the first order Godunov method and the MHM are reported to demonstrate the ability of the scheme to maintain the convergence properties of the deterministic scheme. The Burgers equation is then solved employing a smooth initial, but uncertain, initial condition (§6.2). This case is chosen to demonstrate the ability of the scheme to capture (refining the stochastic space) a discontinuous solution (along the stochastic dimension) even if the discontinuities form during the evolution of a smooth solution. This property is a key feature in the development of numerical schemes for UQ in compressible flows applications. The last test case is the stochastic analysis of the uncertain shock tube problem solving the Euler system of equations in section §6.3. In this case, the statistics of the density are compared to the semi-analytical solution of the Euler equations, considering an uncertain parameter on the initial conditions (see Appendix A).

Systematically in this paper, the spatial norms are computed employing the following definitions

$$\begin{cases} \text{err}_{\mathcal{E}^m}|_{L_p} = ||\mathcal{E}^m(x) - \mathcal{E}^m_{\text{ref}}(x)||_{L_p} = \left(\dfrac{1}{N_x} \displaystyle\sum_{i=1}^{N_x} |\mathcal{E}^m(\bar{u}_i) - \mathcal{E}^m_{\text{ref}}(\bar{u}_i)|^p \right)^{1/p} \\ \text{err}_{\mathcal{E}^m}|_{L_\infty} = ||\mathcal{E}^m(x) - \mathcal{E}^m_{\text{ref}}(x)||_{L_\infty} = \max\limits_i |\mathcal{E}^m(\bar{u}_i) - \mathcal{E}^m_{\text{ref}}(\bar{u}_i)| \,, \end{cases} \tag{58}$$

where the integer $p = 1, 2$ for the L_1 and L_2 norms in the physical space and $\mathcal{E}^m$ indicates a statistical moment, *i.e.* the expectancy or the variance.

6.1 Linear advection

The first test case is the linear advection problem here reported, for $\Omega = [0, 1]$, in its general stochastic formulation

$$\begin{cases} \dfrac{\partial u(x,\xi,t)}{\partial t} + a(\xi,t)\dfrac{\partial u(x,\xi,t)}{\partial x} = 0 \\ u(x,\xi,0) = u_0(x,\xi), \end{cases} \tag{59}$$

where both the advection velocity a and the initial condition u_0 can depend on a random parameter.

Let us consider first the smooth test-case with an initial condition equal to $u_0(x,\xi,t) = sin(4\pi x + 20\xi)$, with the random parameter uniformly distributed $\xi \sim \mathcal{U}[0, 1]$. The problem is solved until the time $t = 1$ with a constant advection velocity equal to $a = 0.1$ and with periodic boundary conditions. The exact

solution can be computed analytically as follows

$$u(x,\xi,1) = sin(4(x-0.1t)\pi + 20\xi) \tag{60}$$

The exact statistics can be computed as function of the $i-$th cell $\mathcal{C}_i = [x_i - \frac{|\mathcal{C}_i|}{2}, x_i + \frac{|\mathcal{C}_i|}{2}]$, integrating first with respect to the stochastic space and then with respect to the space

$$\begin{cases} \mathcal{E}(\bar{u}_i) = \dfrac{1}{|\mathcal{C}_i|}\displaystyle\int_{\mathcal{C}_i}\int_{\Xi} u(x,\xi,1)\,\mathrm{d}\xi\,\mathrm{d}x \\ \mathrm{Var}(\bar{u}_i) = \dfrac{1}{|\mathcal{C}_i|}\displaystyle\int_{\mathcal{C}_i}\int_{\Xi} u^2(x,\xi,1)\,\mathrm{d}\xi - \left(\int_{\Xi} u^2(x,\xi,1)\,\mathrm{d}\xi\right)^2\,\mathrm{d}x. \end{cases} \tag{61}$$

Expressions for both statistics are obtained using the MAPLE software. Numerical simulations are carried out on equally spaced spatial meshes of 51, 101, 201 and 401 points, with $N_t = 200$ time steps and $\Delta t = 5 \times 10^{-3}$.

In figure 4, both the expectancy of the solution 4(a) and the variance 4(a) for the linear advection problem (59) with smooth initial condition and constant advection velocity are reported. The continuous lines indicate the solution obtained via the scheme without compression, while with the dashed lines the solution obtained via the application of the aSI algorithm. In particular, the polynomial reconstruction is taken as a centered second-order polynomial except for the two boundary cells where the stencil is fully shifted into the numerical domain in order to maintain the order of accuracy. In particular, both the Godunov first order scheme and the MHM are reported to show that the numerical scheme is able to preserve the expected order of convergence even with compression. To preserve the formal second order of accuracy, the slope for the MHM is evaluated by a centered approximation without any limiter function. The full solution is obtained on an equally spaced mesh of 128 stochastic cells while the aSI algorithm is applied starting from a coarse level of 16 cell ($m_0 = 4$) to a higher resolution level of 128 cells ($m = 7$) and a threshold equal to $\varepsilon = 10^{-3}$. Note that the finest level is indicated as m. This case is reported in order to show the formal accuracy of the method because the solution is regular enough to minimize the gain associated to the compression of the solution. In particular, the average number of cells employed by the aSI scheme is 126 against the 128 of the full solution. Of course, the level of compression could be easily increased in this case employing a higher order polynomial $\mathcal{P}_j$ for the reconstruction. Remark that, looking at the accuracy, the stochastic reconstruction (quadratic polynomial) is sufficiently accurate with respect to the spatial and time accuracy (second order in the case of MHM). On the contrary, looking at the compression, a higher polynomial order can yield a stronger compression keeping the second order convergence rate.

Let us consider now the linear advection problem (59), that is solved with an uncertain advection ($\xi \sim \mathcal{U}[\frac{1}{5}, \frac{4}{5}]$) velocity defined as

$$a(\xi) = \frac{1}{40}e^{5\xi^2} + \frac{1}{5}, \tag{62}$$

considering a discontinuous initial condition (in the physical space)

$$u(x,\xi,0) = \begin{cases} 1 & \text{if} \quad \dfrac{2}{5} \le x \le \dfrac{3}{5} \\ 0 & \text{if} \quad \text{otherwise.} \end{cases} \tag{63}$$

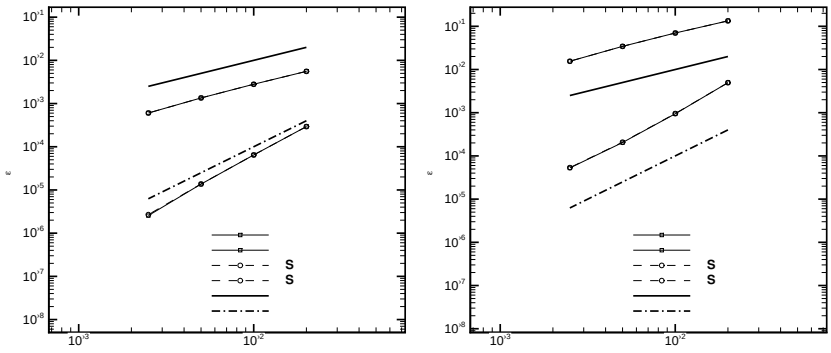

(a) (b)

Figure 4: Spatial convergence for the linear advection problem with smooth initial condition (60). The statistics of the solution (mean (a) and variance (b)) obtained with (aSI) and without (full) compression are reported for both the Godunov first order scheme and the MHM method with a centered slope.

In this case, the problem is solved until the final time of $t = 0.4$ with 200 equal steps of $\Delta t = 2 \times 10^{-3}$. The exact solution is derived for the first two statistical moments employing the following procedure. Referring to the figure 5, starting from the initial condition (defined by the points A_1, A_2, B_2, B_1) the new points (coordinates in the physical space) at the final time ($t = 0.4$) can be computed as follows

$$\begin{cases} A_1'^{,x} = A_1^x + a\left(\frac{1}{5}\right) t = \frac{12}{25} + \frac{1}{100} e^{\frac{1}{5}} \\ A_2'^{,x} = A_2^x + a\left(\frac{1}{5}\right) t = \frac{12}{25} + \frac{1}{100} e^{\frac{1}{5}} \\ B_1'^{,x} = B_1^x + a\left(\frac{1}{5}\right) t = \frac{12}{25} + \frac{1}{100} e^{\frac{16}{25}} \\ B_2'^{,x} = B_2^x + a\left(\frac{1}{5}\right) t = \frac{12}{25} + \frac{1}{100} e^{\frac{16}{25}}. \end{cases} \tag{64}$$

At the final time step, four different regions can be identified (see figure 5(b)). The solution in the external region, where $x \leq A_1'^{,x}$ and $x \geq B_2'^{,x}$, is easily identified as $u(x, \xi, t) = 0$. For the remaining regions, the position of the discontinuity has to be computed. In particular, it is possible to define the two functions $\xi_d^1 = \xi_d^1(x)$ and $\xi_d^2 = \xi_d^2(x)$ as the positions of the discontinuities for each x belonging respectively to the intervals $[A_1'^{,x}, B_1'^{,x}]$ and $[A_2'^{,x}, B_2'^{,x}]$. If x belongs to the interval defined above, the following relations must hold

$$\begin{cases} x = A_1'^{,x} + a\left(\xi_d^1\right) t = \frac{12}{25} + \frac{1}{100} e^{(\xi_d^1)^2} & \text{if} \quad x \in [A_1'^{,x}, B_1'^{,x}] \\ x = A_2'^{,x} + a\left(\xi_d^2\right) t = \frac{17}{25} + \frac{1}{100} e^{(\xi_d^2)^2} & \text{if} \quad x \in [A_2'^{,x}, B_2'^{,x}]. \end{cases} \tag{65}$$

As a consequence, the position of the discontinuities, for a certain physical

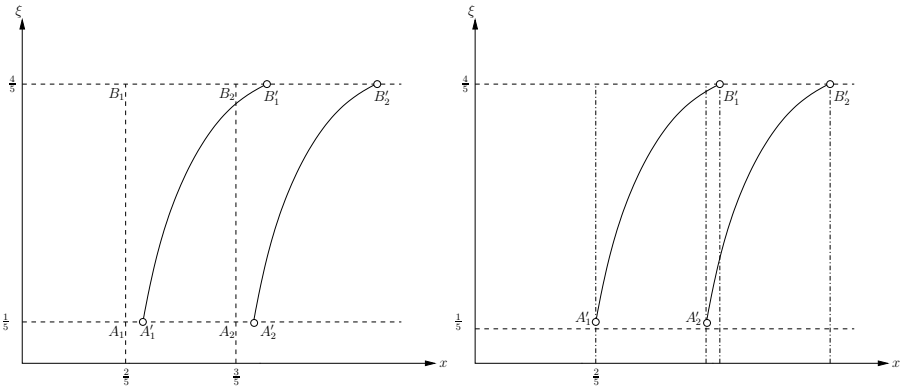

Figure 5: Schematic representation of the evolution between the initial condition (points A_1, A_2, B_1, B_2) and the final condition at time $t = 0.4$ (points A'_1, A'_2, B'_1, B'_2) (a). The regions in which the exact solution should be computed, at the final time $t = 0.4$, are reported in (b).

position can be derived

$$\begin{cases} \xi_d^1 = \xi_d^1(x) = \sqrt{\ln\left(100\left(x - \dfrac{12}{25}\right)\right)} \\ \xi_d^2 = \xi_d^2(x) = \sqrt{\ln\left(100\left(x - \dfrac{17}{25}\right)\right)}. \end{cases} \tag{66}$$

The exact statistics of the physical cell average $\bar{u}_i$ can be computed exactly for each cell $\mathcal{C}_i = \left[x_i - \frac{|\mathcal{C}_i|}{2}, x_i + \frac{|\mathcal{C}_i|}{2}\right]$ (in the limit of $|\mathcal{C}_i| \to 0$). For the mean, they are defined as

$$\mathcal{E}(\bar{u}_i) = \begin{cases} 0 & \text{if} \quad x_i \leq A_1'^{,x} \text{ or } x_i \geq B_2'^{,x} \\ \dfrac{5}{3}\left(\xi_d^1(x_i) - \dfrac{1}{5}\right) & \text{if} \quad x_i \in [A_1'^{,x}, A_2'^{,x}] \\ \dfrac{5}{3}\left(\xi_d^1(x_i) - \xi_d^2(x_i)\right) & \text{if} \quad x_i \in [A_2'^{,x}, B_1'^{,x}] \\ \dfrac{5}{3}\left(\dfrac{4}{5} - \xi_d^2(x_i)\right) & \text{if} \quad x_i \in [B_1'^{,x}, B_2'^{,x}]. \end{cases} \tag{67}$$

Concerning the variance, they can be obtained as (and not as $\text{Var} = \mathcal{E}((\bar{u}_i)^2) - (\mathcal{E}(\bar{u}_i))^2$)

$$\text{Var} = \mathcal{E}(\bar{u}_i) - (\mathcal{E}(\bar{u}_i))^2 \quad \forall x_i \in [0,1], \tag{68}$$

because in this specific case ($\bar{u}(x, \xi, t) = 1$)

$$\int_\Xi \bar{u}(x_i, \xi, t)^2 p(\xi) \mathrm{d}\xi = \int_\Xi \bar{u}(x_i, \xi, t) p(\xi) \mathrm{d}\xi = \mathcal{E}(\bar{u}_i). \tag{69}$$

In figure 6, the spatial convergence for the aSI scheme and for the full scheme, employing only the MHM with the superbee limiter (48), are reported for the

mean 6(a) and the variance 6(b) (L_2 norms). Similar curves are obtained for L_1 and L_∞ norms but are not reported here for brevity. The computations are performed over equally spaced meshes in the physical space Ω with 51, 101, 201, 401 and 601 points. The aSI scheme is applied with a coarsest level of 16 cells ($m_0 = 4$), a finest level of 256 stochastic cells ($m = 4$) and a threshold equal to $\varepsilon = 10^{-3}$. The polynomial reconstruction is the quadratic polynomial with and without ENO selection of the stencil. The average number of stochastic cells employed is equal to 39 when the ENO selection is employed and 40 with the centered stencil.

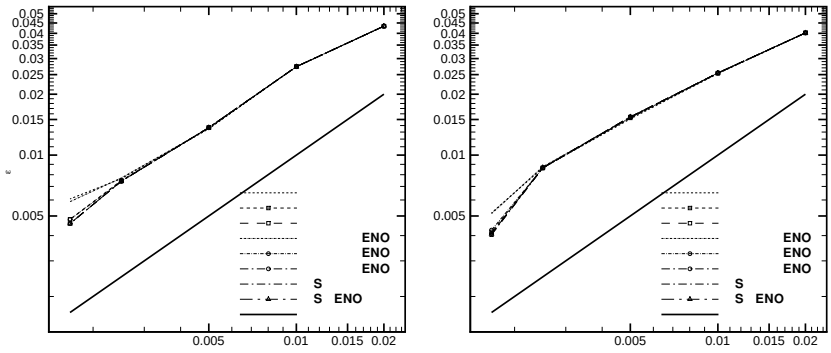

(a) (b)

Figure 6: Spatial convergence for the linear advection problem with discontinuous initial condition (63). The statistics of the solution (mean (a) and variance (b)) obtained with (aSI) and without (full) compression are reported for the MHM method with the superbee limiter (48).

The figure 6 shows that the aSI scheme is able to preserve the accuracy and the order of convergence of the full scheme with a reduction of the computational cost with respect to the full solution obtained over a grid of 256 cells ($m = 8$). The aSI scheme requires a computational effort equivalent to a computation carried out on about 40 equally spaced stochastic cells. The full solutions on 32 ($m = 5$) and 64 ($m = 6$) cells are then reported in order to compare the efficiency of the scheme with respect to a solution obtained with a similar computational effort. However, the aSI scheme performs better with respect to both the full solution at 32 and 64 cells. Moreover, the quality with respect to the full solution of 256 cells is only slightly degraded. In figures 7 and 8, the statistics of the solution are reported over the entire physical space (the mesh of 601 points) and compared to the exact solution (see (67)) obtained on 2001 equally spaced points in the physical space. The solutions obtained with the full scheme with 32 and 64 stochastic cells exhibit the well-known staircase phenomenon, i.e. in presence of discontinuous solutions the statistics are constituted by a series of *plateau*. The presence of the plateau is due to the lower resolution associated to the discretization of the stochastic space with respect to the resolution of the physical space. The staircase phenomenon is more evident for the coarser case (32 cells), reduces slightly with 64 cells, and disappear with 256 cells. The

aSI scheme automatically refines the space where a higher resolution is required. Remark that the staircase problem disappears by using aSI even if the (average) number of cells employed is lower than 64 (see figure 7(b) and 8(b)).

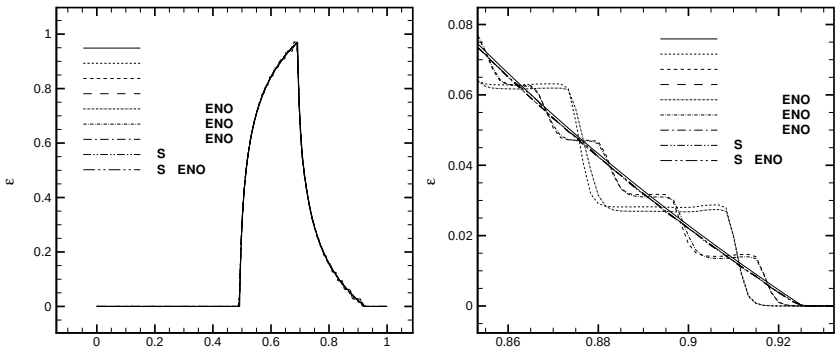

(a) (b)

Figure 7: Expectancy for the cell averaged solution of the linear advection equation with discontinuous initial condition (63) at the final time $t = 0.4$. The whole physical domain is represented in (a), while in the figure (b) a zoom in the shock region is reported. The mesh is constituted by 601 equally spaced points.

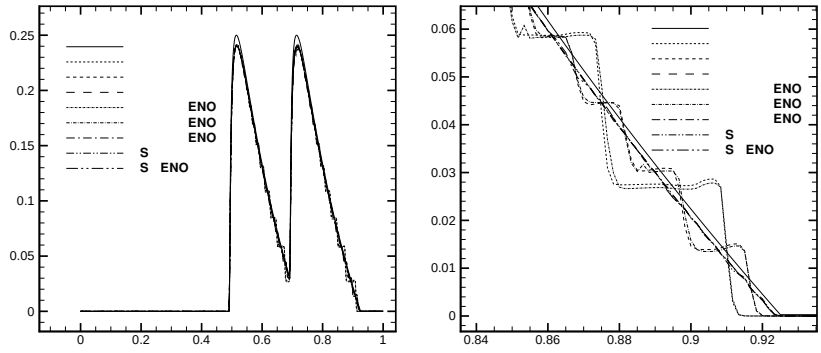

(a) (b)

Figure 8: Variance for the cell averaged solution of the linear advection equation with discontinuous initial condition (63) at the final time $t = 0.4$. The whole physical domain is represented in (a), while in the figure (b) a zoom in the shock region is reported. The physical mesh is constituted by 601 equally spaced points.

The ability of aSI scheme to refine only locally the space allows to increase locally the resolution along the stochastic space. In figure 9, the distribution of

the stochastic cells over Ω at the final time step $t = 0.4$ is reported. It is evident that the higher computational effort is located in the region of the strong gradients; comparing the figure 8 and 9, it is evident that the two peaks associated to the local higher computational effort (in terms of stochastic cells) corresponds to the two peaks in the variance of the solution. In figure 9, the number of points employed by the aSI scheme with and without the ENO selection of the stencil are also reported. The ENO selection of the stencil reduces the number of cells employed. Morevoer, comparing the average number of stochastic cells employed for each computation, it is evident that the efficiency of the ENO selection increases with the spatial resolution. This is due to the global representation of the solution $u(x, \xi, t)$ over cells $\mathcal{C}_i \times \Xi_j$. Higher is the spatial resolution, sharper are the resulting discontinuities, so the ENO becomes more useful in order to gain in terms of accuracy (with the SI algorithm) and in terms of compression capabilities (with the TE algorithm). Figure 9(b) displays that for too coarse spatial resolution, the ENO selection of the stencil can be negative in terms of both accuracy and compression. The solution becomes smoother and smoother by decreasing the spatial resolution, so a centered stencil becomes the best choice.

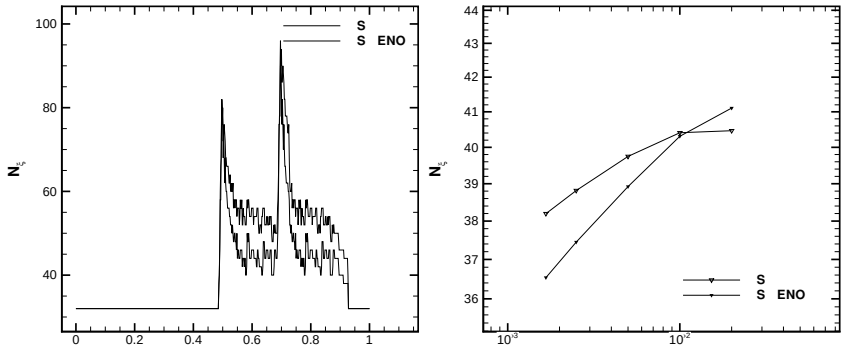

(a) (b)

Figure 9: Evolution of the number of stochastic cells employed in each physical location for the aSI scheme with and without the ENO reconstruction (a) for the linear advection equation with discontinuous initial condition. The average number of stochastic cells employed by the aSI scheme as function of the physical space resolution is reported in (b).

6.2 Inviscid Burgers equation

In this section, the aSI algorithm is applied to the solution of the inviscid Burgers equation

$$\frac{\partial u(x,\xi,t)}{\partial t} + \frac{\partial f(u(x,\xi,t))}{\partial x} = 0 \quad x \in [0,1] \quad \text{and} \quad t \in [0,T], \tag{70}$$

where the flux function is defined as $f = f(u(x,\xi,t)) = \frac{1}{2}u^2(x,\xi,t)$.

We assume the following uncertain initial condition, with the random parameter uniformly distributed $\xi \sim \mathcal{U}[0,1]$,

$$u(x,\xi,0) = \begin{cases} H(\xi) & \text{if} \quad x \in [A_1^x, A_2^x] \\ 0 & \text{if} \quad \text{otherwise.} \end{cases} \tag{71}$$

The initial condition is represented by a hat function with a different amplitude dependent (non linearly) from the random parameter, $H(\xi) = \frac{1}{3}\xi^2 + \frac{1}{100}\xi + \frac{9}{10}$. To obtain the exact solution it is necessary to consider the two elementary solutions of the Riemann problem of the inviscid Burgers equation (see [23] for further details). The first case at the left of the hat function ($x = \frac{1}{10}$) is the Riemann problem with $u_l < u_r$ that admits as solution a rarefaction wave (depending on the uncertainty parameter) as follows

$$u(x,\xi,t) = \begin{cases} 0 & \text{if} \quad x \leq A_1^x \\ F(x) & \text{if} \quad x \in [A_1^x, A_1^x + H(\xi)t] \\ H(\xi) & \text{if} \quad x > A_1^x + H(\xi)t, \end{cases} \tag{72}$$

where the solution inside the rarefaction wave is $F(x) = (x + A_1^x)/t$.

Knowing the function $H(\xi)$, the exact solution for the uncertain rarefaction wave can be computed. Let us consider now the right of the hat initial function ($x = \frac{1}{2}$), where the solution of the Riemann problem is a shock wave traveling with an uncertain speed $s = H(\xi)/2$. The complete solution of the Riemann problem is then

$$u(x,\xi,t) = \begin{cases} H(\xi) & \text{if} \quad x < A_2^x + st \\ 0 & \text{if} \quad x > A_2^x + st. \end{cases} \tag{73}$$

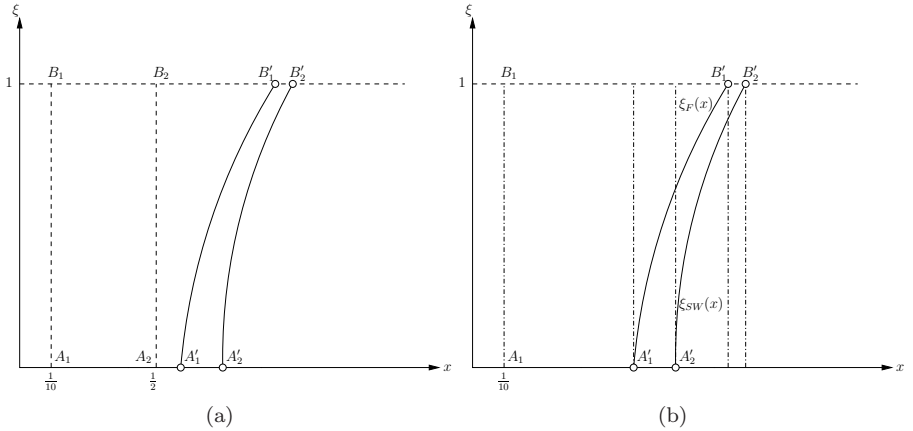

Figure 10: Schematic representation of the evolution between the initial condition (points A_1, A_2, B_1, B_2) and the final condition at time $t = 0.6$ (points A'_1, A'_2, B'_1, B'_2) (a). The regions in which the exact solution should be computed, at the final time $t = 0.6$, are reported in (b).

We solve the problem (70) until a time equal to $T = 0.6$, with the initial condition (71) defined by $A_1^x = B_1^x = \frac{1}{10}$ and $A_2^x = B_2^x = \frac{1}{2}$. The solution

appears as sketched in figure 10, where the tail of the fan is at rest ($x = \frac{1}{10}$) while the position of the head is a function of the random parameter and its value is bounded between the slower moving fan ($A_1'^{,x} = \frac{1}{10} + H(0)t$) and the fast moving fan ($B_1'^{,x} = \frac{1}{10} + H(1)t$). The random parameter corresponding to a physical position $x \in [A_1'^{,x}, B_1'^{,x}]$ can be found after some algebraic manipulations analytically, by solving for ξ the equation $x = A_1^x + H(\xi)t$ for $A_1'^{,x} \leq x \leq B_1'^{,x}$, $\xi_F = \xi_F(x)$ (see figure 10 for the locus ξ_F). Following a similar procedure, the value of the random parameter corresponding to the shock position $\xi_{SW} = \xi_{SW}(x)$ can be found analytically, solving for ξ the equation $x = A_2^x + \frac{1}{2}H(\xi)t$ for $A_2'^{,x} \leq x \leq B_2'^{,x}$.

The statistics of the solution can be computed analytically for each cell $\mathcal{C}_i$ as follows. For the expectancy of the physical cell averaged value $\bar{u}_i$, it holds that

$$\mathcal{E}(\bar{u}_i) = \begin{cases} 0 & \text{if} \quad x_i \leq A_1^x \text{ or } x_i \geq B_2'^{,x} \\ F(x_i) & \text{if} \quad x_i \in [A_1, A_1'^{,x}] \\ \displaystyle\int_0^{\xi_F(x_i)} H(\xi)\mathrm{d}\xi + F(x_i)(1-\xi_F(x_i)) & \text{if} \quad x_i \in [A_1'^{,x}, A_2'^{,x}] \\ \displaystyle\int_{\xi_F(x_i)}^{\xi_{SW}(x_i)} H(\xi)\mathrm{d}\xi + F(x_i)(1-\xi_F(x_i)) & \text{if} \quad x_i \in [A_2'^{,x}, B_1'^{,x}] \\ \displaystyle\int_{\xi_{SW}(x_i)}^{1} H(\xi)\mathrm{d}\xi & \text{if} \quad x_i \in [B_1'^{,x}, B_2'^{,x}]. \end{cases} \tag{74}$$

All the integrals in the equation (74) can be computed analytically.

Moreover, the variance is easily analytically computed, due to the polynomial behavior of $H(\xi)$, as follows

$$\mathrm{Var}(\bar{u}_i) = \begin{cases} 0 & \text{if} \quad x_i \leq A_1'^{,x} \text{ or } x_i \geq B_2'^{,x} \\ \displaystyle\int_0^{\xi_F(x_i)} H^2(\xi)\mathrm{d}\xi + F^2(x_i)(1-\xi_F(x_i)) - \mathcal{E}^2(\bar{u}_i) & \text{if} \quad x_i \in [A_1'^{,x}, A_2'^{,x}] \\ \displaystyle\int_{\xi_F(x_i)}^{\xi_{SW}(x_i)} H^2(\xi)\mathrm{d}\xi + F^2(x_i)(1-\xi_F(x_i)) - \mathcal{E}^2(\bar{u}_i) & \text{if} \quad x_i \in [A_2'^{,x}, B_1'^{,x}] \\ \displaystyle\int_{\xi_{SW}(x_i)}^{1} H^2(\xi)\mathrm{d}\xi - \mathcal{E}^2(\bar{u}_i) & \text{if} \quad x_i \in [B_1'^{,x}, B_2'^{,x}]. \end{cases} \tag{75}$$

The (stochastic) inviscid Burgers problem (70) is solved over a set of equally spaced physical meshes with 51, 101, 201, 401 and 601 points. The time space is discretized using 600 time steps of constant length $\Delta t = 1 \times 10^{-3}$. The error norms in L_2, with respect to the exact stochastic solution (see equations (74) and (75)), are reported in figure 11. Similar results are obtained for L_1 and L_∞ norms, but are not reported here for brevity. The reference solution is the full computation performed with the SI scheme and a 256 ($m = 8$) equally spaced stochastic cells. This solution is compressed by means of the aSI scheme with a coarsest level of $m_0 = 4$ and a finest level of $m = 8$ with a threshold equal to $\varepsilon = 10^{-4}$. For both the full SI and the aSI schemes the computations are performed employing quadratic polynomial reconstruction with and without the ENO selection of the stencil. For each computation, the average number of

stochastic cells is evaluated obtaining the equivalent number of equally spaced stochastic cells (with the same computational cost). The evolution of the number of stochastic cells associated to the different (physical) spatial resolutions are reported in figure 14(b) for the aSI scheme with and without the ENO procedure. Moreover, SI scheme is applied over 16 ($m = 4$) and 32 ($m = 5$) equally spaced stochastic cells. These resolutions are chosen because the average number of stochastic cells employed by the aSI scheme varies between these values. The SI scheme fails to converge with the expected first order slope both with and without the ENO, because of the appearance of the staircase phenomenon. The stochastic resolution is not high enough with respect to the physical resolution, as evident looking at the three last spatial resolutions in figure 11.

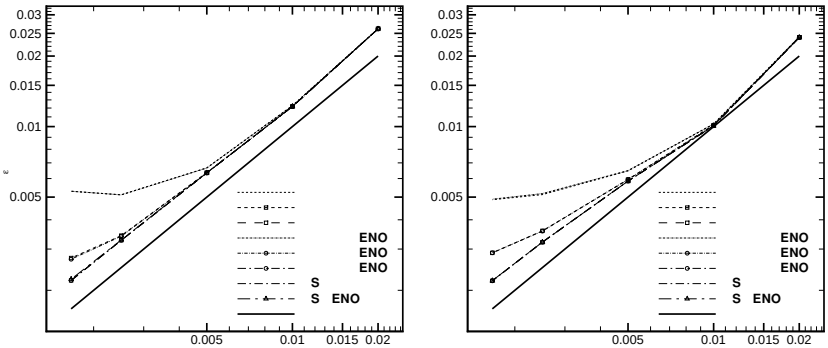

(a) (b)

Figure 11: Spatial convergence for the Burgers equation with an uncertain hat initial condition (71). The statistics of the solution (mean (a) and variance (b)) obtained with (aSI) and without (full) compression are reported for the MHM method with superbee limiter (48).

The staircase phenomenon is evident in figures 12 and 13, where the expectancy and the variance of the solution are reported over the 601 points physical mesh (the exact solution is evaluated over a mesh of 2001 equally spaced points). In particular, figures 12(b) and 13(b) show a zoom of the curves in the region, where the (uncertain) shock wave propagates (see figure 10). As expected, increasing the number of stochastic cells, even equally spaced, reduces the staircase phenomenon (from 16 to 32 cells). It disappears at 256 cells. Note that the aSI scheme, with an overall computational cost similar to the two coarse full simulations, produces better results (without the appearance of the staircase phenomenon) concentrating the computational effort, *i.e.* the number of cells, in the regions where the solution is less regular. The capability to refine and derefine during the simulation following the evolution of the solution in the physical/stochastic space makes the aSI scheme more efficient, yielding results that nearly coincide with the full reference solution.

As already discussed for the solution of the linear advection equation with discontinuous initial condition, the presence of the ENO selection of the stencil makes the computations progressively more efficient increasing the physical

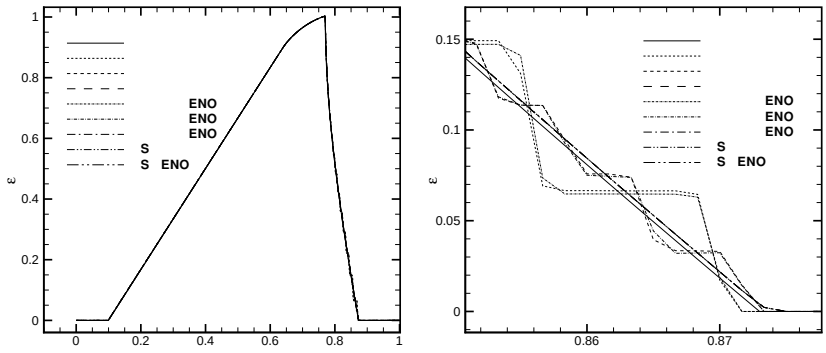

(a) (b)

Figure 12: Expectancy for the cell-averaged solution of the inviscid Burgers equation at the final time $t = 0.6$. The whole physical domain is represented in (a), while in figure (b) a zoom in the shock region is reported. The physical mesh is constituted by 601 equally spaced points.

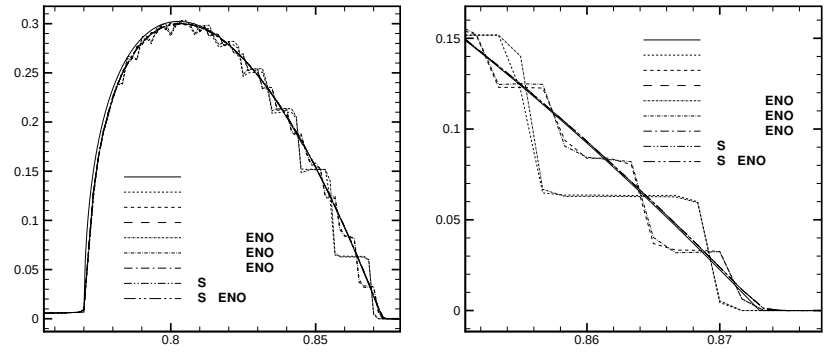

(a) (b)

Figure 13: Variance for the cell-averaged solution of the inviscid Burgers equation at the final time $t = 0.6$. Two different zooms in the shock region are reported. The physical mesh is constituted by 601 equally spaced points.

resolution. This effect is evident in figure 14(b), where the (average) number of stochastic cells employed is reported as a function of the physical resolution. In figure 14(a), the direct comparison between the aSI scheme with and without the ENO selection of the stencil over the finest 601 points physical mesh is shown. With lower resolution meshes, there is no advantage in using the ENO procedure due to the representation of the solution over cells in the overall physical/stochastic space. However, the slope associated to the average number of stochastic cells shows that the solutions are represented by a narrow discontinuity (due to the increase of the spatial resolution). As a consequence,

the non-oscillatory interpolation helps to avoid the so-called *pollution* of the stencil, *i.e.* the propagation of the interpolation error in the neighboring cells of a discontinuity. Again, the combination of the aSI scheme and the use of the ENO procedure for the polynomial interpolation, becomes even more efficient as the spatial resolution is increased. This is a desired property for any intrusive UQ scheme.

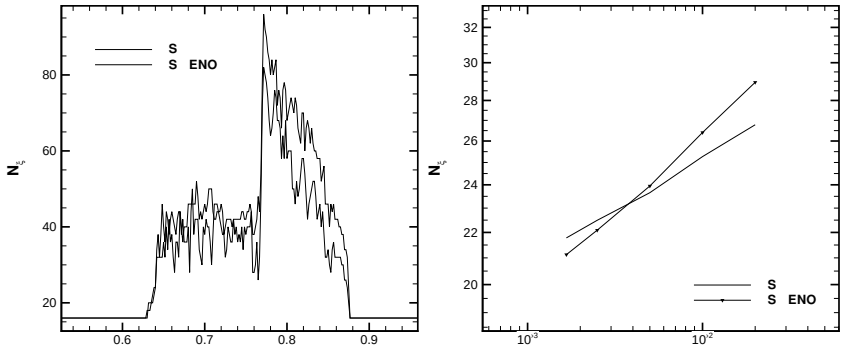

(a) (b)

Figure 14: Evolution of the number of stochastic cells employed for each physical location for the aSI scheme with and without the ENO reconstruction (a) for the inviscid Burgers equation. The average number of stochastic cells employed by the aSI scheme as a function of the physical space resolution is reported in (b).

In the following section, the aSI scheme is applied to non linear system of stochastic partial differential equations.

6.3 Uncertain shock tube

In this section, the solution of the uncertain shock tube problem is reported. The problem can be modeled by the well-known 1D Euler equations

$$\frac{\partial \mathbf{u}}{\partial t} + \nabla \cdot \mathbf{f}(\mathbf{u}) = \mathbf{0} \tag{76}$$

where the vector of conservative variables, the density ρ, the momentum $m = \rho u$ and the total Energy E^t, $\mathbf{u} \in \mathbb{R}^3$ and the flux vector $\mathbf{f}(\mathbf{u}) \in \mathbb{R}^3$ are

$$\mathbf{u} = \begin{pmatrix} \rho \\ m \\ E^t \end{pmatrix} \quad \mathbf{f}(\mathbf{u}) = \begin{pmatrix} m \\ \dfrac{m^2}{\rho} + \Pi(\mathbf{u}) \\ \dfrac{m}{\rho}\left(E^t + \Pi(\mathbf{u})\right). \end{pmatrix} \tag{77}$$

The pressure $\Pi(\mathbf{u})$ (as function of the conservative variables) can be derived for a polytropic ideal gas as follows

$$\Pi(\mathbf{u}) = (\gamma - 1)\left(E^t - \frac{1}{2}\frac{|m^2|}{\rho}\right). \tag{78}$$

The initial condition for the uncertain shock tube problem is derived from the classical Sod test case [25], where an uncertainty of the density at the left state ($x < x_d$ for $t = 0$) is introduced:

$$\mathbf{u}_L(x,\xi,t) = \begin{pmatrix} \rho_L(\xi) \\ 0 \\ \dfrac{p_L}{\gamma - 1} \end{pmatrix} \quad \mathbf{u}_R(x,\xi,t) = \begin{pmatrix} \rho_R \\ 0 \\ \dfrac{p_R}{\gamma - 1}. \end{pmatrix}, \tag{79}$$

In particular, the density on the left state is dependent from an uniformly distributed random parameter $\xi \sim \mathcal{U}[0,1]$: $\rho_L(\xi) = 0.3 + 1.6\xi$. The values of the pressures are $p_L = 1$ and $p_R = 0.1$, while the right value of the density is $\rho_R = 0.125$. The total energy E^t is obtained (considering the gas at the rest in the whole domain) as a function of the local pressure and the ratio between specific heats, that for a diatomic gas can be assumed equal to $\gamma = 1.4$.

As pointed out by Toro [24], analyzing the eigenvalue structure of the Euler equations, the Riemann problem for the 1D Euler equations (see figure 15) generates (for $t > 0$) four states, where two are not known (variables are indicated with a star in the following). The Riemann problem for the solution of the 1D Euler equation can be reduced to the solution of a single non-linear algebraic equation for the pressure in the star region $p^\star$ from which the other quantities can be computed. With an uncertain shock tube problem, the dependence of $p^\star$ from the random parameter $p^\star = p^\star(\xi)$ should be considered. Unfortunately, this dependence cannot be computed explicitly. In this paper, only the case involving a left moving rerefaction fan and a right moving shock wave are considered. Moreover, initial conditions (79) produce this wave structure for all the random parameter taken into account. The problem is further complicated by the presence of complex functions that should be integrated to compute the exact statistics required. The solution strategy employed is the following. For each physical location, where the exact statistics should be computed, the solution along the stochastic space is divided into smooth regions (where the numerical quadrature with a large number of points produces fair well-converged results even for non-polynomial functions). The main issue is to determine the location of a discontinuity. This task can be accomplished solving an algebraic non-linear equation for the random parameter that can be formulated to involve all (but not only) the derivative available for the solution of the deterministic Riemann problem. After the subdivision of the random space in more regions, where the quadrature can be done numerically without accuracy loss (to the desired global accuracy), the statistics are computed in order to obtain the desired reference solutions.

Details of the numerical procedure to obtain the reference solution of the stochastic Riemann problem are reported in the Appendix A.

Simulations are performed over a physical domain $\Omega = [-\frac{1}{5}, \frac{6}{5}]$ until a final time $t = 0.31$ with the position of the diaphragm equal to $x_d = 0.42$. The time space is divided in 6200 equal time steps of length $\Delta t = 5 \times 10^{-5}$. The simulations are carried out over equally spaced meshes of 201, 401, 801 and 1001 points employing the aSI scheme based on the MHM with a van Leer limiter (see equation (49)).

In figure 16, the spatial convergence is reported for both the mean (16(a)) and the variance (16(b)) in L_2 for the density ρ. The aSI method is obtained

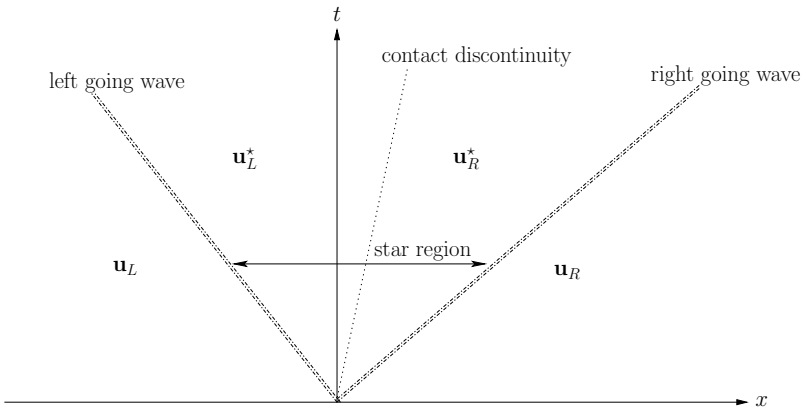

Figure 15: Riemann wave structure for the 1D Euler equation.

with a coarsest level of 4 ($m_0 = 2$) cells and a finest level of 256 ($m = 8$) stochastic cells with $\varepsilon = 10^{-4}$, while the reference solution is the full SI scheme with 256 cells. The aSI scheme has used an average number of stochastic cells between the two levels $m = 5$ and $m = 6$ (see figure 19(b)), so the other solutions are computed by means of the SI scheme for comparison. For all the schemes, both the centered second order polynomial reconstruction and the non-linear ENO one are used. The difference between the two polynomial reconstructions is difficult to appreciate because the spatial resolution is too poor for a sharp representation of the discontinuities. In this sense, there is no advantage in using the ENO reconstruction (for the aSI scheme and the SI scheme). The first order of convergence is attained for the expectancy of the density ρ, while, even with the SI scheme, the variance exhibits a lower rate of convergence 16(b). This behavior clearly indicates that even the solution employing 256 stochastic cells is not fully converged for moments higher than the expectancy.

However, the aSI scheme displays the required properties: it saves the order of accuracy of the full SI scheme, both for mean and variance (see figure 16), and the degradation of the accuracy is strongly limited. Moreover, as already shown in the previous numerical results, the phenomenon of the staircase approximation of the statistics is prevented by the adaptation in the stochastic space. As shown in figure 17, note that all the numerical solutions are very similar to the exact solution 17(a) obtained over a mesh of 2001 equally spaced points in the physical space. By zooming (17(b)), the presence of the typical staircase phenomenon for both the SI scheme with 32 and 64 stochastic cells appears. The solution obtained with the aSI scheme agree very well with its full counterparts.

As already demonstrated for the mean, even for the variance, the presence of the staircase approximation is prevented by the refinement of the stochastic space (see figure 18). Even if curves nearly coincide in figure 18(a), in the shock region the presence of the typical step pattern is evident for the full SI solution with 32 and 64 equally spaced stochastic cells (see 18(b)).

The lower order of convergence attained for the variance, even for the non compressed solution, highlights that the error in the stochastic space dominates the global error. As already demonstrated, the efficiency of the ENO selection

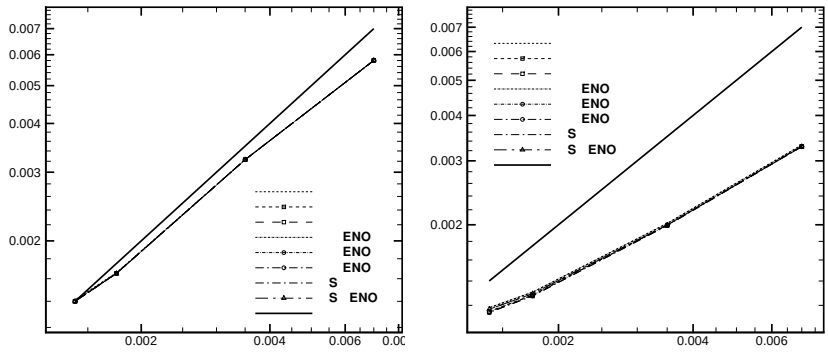

(a) (b)

Figure 16: Spatial convergence for the stochastic shock tube problem equation with uncertain initial condition (79). The statistics of the solution (mean (a) and variance (b)) obtained with (aSI) and without (full) compression are reported for the MHM method with van Leer limiter (49).

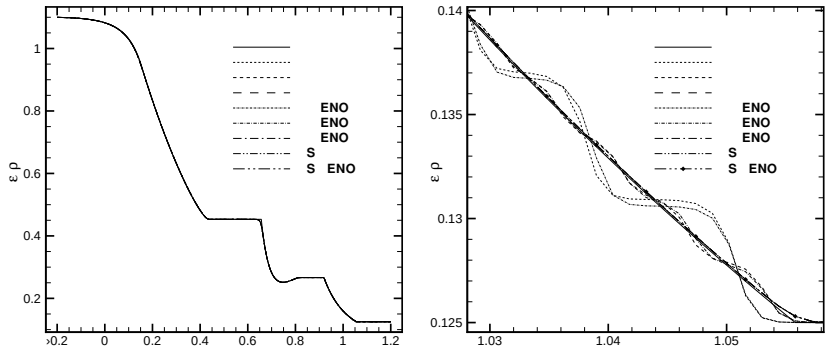

(a) (b)

Figure 17: Density Expectancy for the cell averaged solution of the uncertain shock tube problem at the final time $t = 0.31$. The whole physical domain is represented in (a), while in the figure (b) a zoom in the shock region is reported. The physical mesh is constituted by 1001 equally spaced points.

of the stencil is related to the sharp representation of the discontinuities. In this case, the results with and without the ENO selection of the stencil are very similar. No advantages, even in term of compression, are observed. This issue is evident in figure 19(a), where the number of stochastic cells, along the physical domain, are reported. The region associated to the discontinuity spreads over a larger domain and, globally, the presence of non-centered stencils degradates the quality of prediction. This issue is well known in the ENO literature [26]. A possible cure, outside the scope of the present paper, would be the introduction

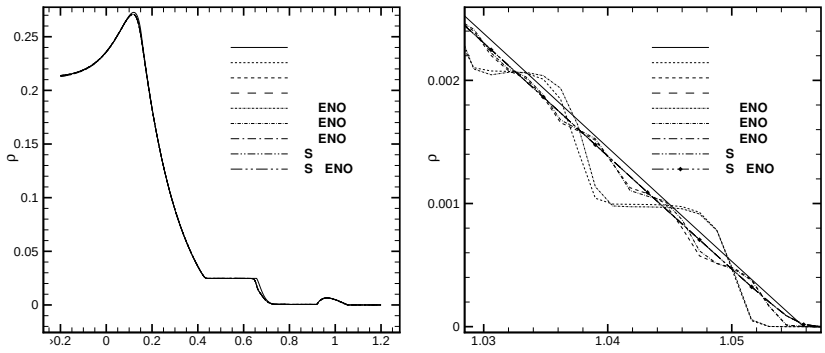

(a) (b)

Figure 18: Density Variance for the cell averaged solution of the uncertain shock tube problem at the final time $t = 0.31$. The whole physical domain is represented in (a), while in the figure (b) a zoom in the shock region is reported. The physical mesh is constituted by 1001 equally spaced points.

of WENO type of interpolation. Employing a WENO type of interpolation, the correct centered stencil could be recovered without strong degradation of the prediction (the author already introduced a WENO interpolation in [10] in the context of the MR point-value setting).

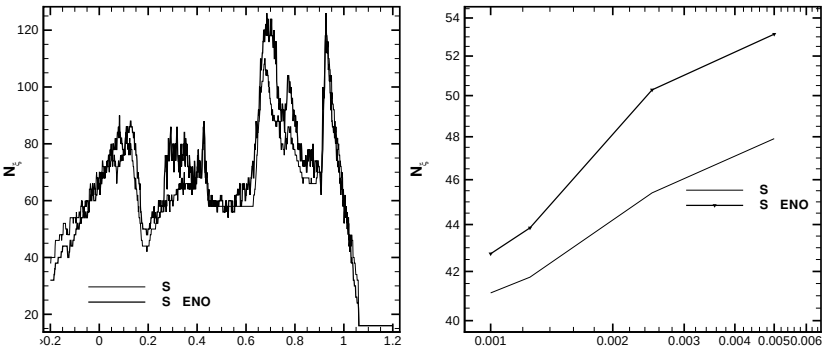

(a) (b)

Figure 19: Evolution of the number of stochastic cell employed for each physical location for the aSI scheme with and without the ENO reconstruction for the shock tube problem. The average number of stochastic cells employed by the aSI scheme as function of the physical space resolution has been reported in (b).

The evolution of the average number of stochastic cells employed by the aSI scheme with and without the ENO interpolation is reported in 19(b). In this case, there is no intersection between the two curves, revealing that in this

case the ENO interpolation gives no advantage, even for high physical space resolutions.

7 Concluding remarks

In this paper, a novel adaptive intrusive numerical scheme for Uncertainty Quantification has been presented. The classical MR Harten framework, in its cell average setting, has been here extended to include the dependence from a generic probability density function. Moreover, an original algorithm has been developed to obtain the solution at the finest resolution level starting from the coarsest one. The aim is to obtain, at the same time, a saving in memory requirements and in the computational cost associated to the true model evaluation of the system. This general algorithm has been coupled with the Semi-Intrusive (SI) scheme for UQ proposed by Abgrall and Congedo [7]. The overall numerical scheme is the so-called adaptive-SI scheme. We demonstrated that it preserves the convergence properties of the original SI scheme with a strong saving in term of computational cost. Different test-cases have been presented to demonstrate the efficiency and the accuracy properties of the aSI scheme. The linear advection equation has been solved for initial smooth and discontinuous solution to demonstrate the capability of the stochastic scheme to preserve the accuracy related to the deterministic MUSCL-Hancock method (MHM). A second test-case has been focused on the inviscid Burgers equation. We demonstrated the capability of the method to automatically refine/derefine following the changes in the regularity of the solution in the coupled stochastic/physical space. In particular, a smooth solution has been considered, in the stochastic space, as initial condition, where shock waves velocities are directly related to the parameter in the stochastic space. The final test case proposed has been the Euler system of equation to solve an uncertain shock tube problem. The aSI scheme has been demonstrated to be efficient also in the case of vectorial problems. For the computation of the convergence curves, an original strategy for the semi-analytical solution of the stochastic shock tube problem has been also developed following and extending the classical numerical procedure for the solution of the Riemann problem for the Euler equations. This paper constituted the first effort to introduce a MR framework into the SI method. The generality of the approach is not limited to second order scheme, but can be easily extended to higher order numerical formulation for the physical space and time discretizations. In the present work, both the linear and non-linear MR framework have been presented in which the selection of the stencil to obtain the reconstruction operators can be obtained by a data-dependent procedure. The ENO selection of the stencil has been also introduced. Considering the numerical results presented, note that the advantages related to the non-linear schemes are very limited. This issue is related not to the non-linear procedure itself but to the peculiarity of the SI scheme that produces representations of the solution in a combined physical stochastic space. The representation of discontinuous solution along the stochastic space can recover a smoother behavior when the physical spatial resolution is not high enough. This has been demonstrated showing that the importance of the ENO scheme increases with the physical space resolution. To improve the global properties of the scheme, two further steps seem useful. The first is the introduction of the WENO reconstruction instead of the ENO interpolation recovering the correct stencil in all the regions in which the solution is

smooth, as it has been already presented for the point-value setting [10]. The other step could be to increase the polynomial order for the reconstruction. This should improve both accuracy and compression capabilities. The extension and the analysis of the aSI scheme for a moderate number of dimension is actually underway.

Acknowledgements

Rémi Abgrall and Gianluca Geraci have been supported by the ERC Advanced Grant ADDECCO N°226316. The authors greatly acknowledge also the Associated Team AQUARIUS (Joint team from INRIA and Stanford University) for funding the stay of Gianluca Geraci and Pietro Marco Congedo at Stanford University in which part of the present work has been conceived. The authors thank the support of the French Agence Nationale de la Recherche (ANR) under reference ANR-11-MONU-0008.

A Accurate numerical solution for the 1D stochastic Riemann problem for the Euler equations

In this section, let us illustrate the numerical procedure to obtain the reference solution for the stochastic shock tube problem (the interesting reader may refer to [24] for a complete description of the deterministic problem). Let us consider a deterministic Riemann problem for the 1D Euler equations, in particular the case of a left going rarefaction wave and a right moving shock wave. This assumption do not pose any limitation on the general procedure for the solution of the stochastic problem presented here.

The solution of the deterministic Riemann problem (for gas initially at the rest) consists in solving a non-linear equation for the pressure in the region between the shock and the contact discontinuity. Remark that each quantity is dependent on the random parameter. In the deterministic case, the random parameter is obviously assumed as a constant. In the following, the explicit dependence of each quantity with respect the random parameter ξ is explicitly reported for the uncertain initial left stat (see equation (79)). However the dependence of all the quantities from the random parameter must be considered redundant if the deterministic case is of interest because in that case all the uncertain parameters assume a fixed value. The non-linear equation to solve for the pressure in the star region $p^\star$ is the following

$$\begin{aligned} f(p^\star(\xi),\mathbf{u}_L(\xi),\mathbf{u}_R) &= f_L(p^\star(\xi),\mathbf{u}_L(\xi)) + f_R(p^\star(\xi),\mathbf{u}_R) \\ &= \frac{2a_L(\xi)}{\gamma-1}\left[\left(\frac{p^\star(\xi)}{p_L}\right)^{\frac{\gamma-1}{2\gamma}} - 1\right] + (p^\star(\xi)-p_R)\left[\frac{\frac{2}{(\gamma+1)\rho_R}}{p^\star(\xi)+\frac{\gamma-1}{\gamma+1}p_R}\right]^{\frac{1}{2}} = 0, \end{aligned} \tag{80}$$

with the speed of sound $a_L(\xi) = \sqrt{\gamma\frac{p_L}{\rho_L(\xi)}}$.

The equation (80) is solved by means of an iterative Newton-Raphson scheme following [24]

$$\begin{cases} \Delta p^\star = -\left(\dfrac{\mathrm{d}f(p^\star(\xi),\mathbf{u}_L(\xi),\mathbf{u}_R)}{\mathrm{d}p^\star}\Big|_{p^\star(\xi)=p_k^\star(\xi)}\right)^{-1} f(p_k^\star(\xi),\mathbf{u}_L(\xi),\mathbf{u}_R) \\ p_{k+1}^\star(\xi) = p_k^\star(\xi) + \Delta p^\star. \end{cases} \tag{81}$$

The initial condition is systematically $p_0^\star = \frac{p_L+p_R}{2}$) and $\Delta p^\star \leq 10^{-14}$ is chosen as convergence criterion.

Derivative of the function $f(p^\star(\xi),\mathbf{u}_L(\xi),\mathbf{u}_R)$ with respect to $p^\star$ that can be computed as follows

$$\begin{cases} \dfrac{\mathrm{d}f(p^\star(\xi),\mathbf{u}_L(\xi),\mathbf{u}_R)}{\mathrm{d}p^\star(\xi)} = \dfrac{\mathrm{d}f_L(p^\star(\xi),\mathbf{u}_L(\xi))}{\mathrm{d}p^\star} + \dfrac{\mathrm{d}f_R(p^\star(\xi),\mathbf{u}_R)}{\mathrm{d}p^\star} \\ \dfrac{\mathrm{d}f_L(p^\star(\xi),\mathbf{u}_L(\xi))}{\mathrm{d}p^\star} = \dfrac{1}{\gamma p^\star(\xi)}\sqrt{\gamma\dfrac{p_L}{\rho_L}}\left(\dfrac{p^\star(\xi)}{p_L}\right)^{\frac{\gamma-1}{2\gamma}} \\ \dfrac{\mathrm{d}f_R(p^\star(\xi),\mathbf{u}_R)}{\mathrm{d}p^\star} = \dfrac{2}{(\gamma+1)\rho_R\left(p^\star(\xi)+\frac{\gamma-1}{\gamma+1}p_R\right)}\left[1-\dfrac{(p^\star(\xi)-p_R)}{\left(p^\star(\xi)+\frac{\gamma-1}{\gamma+1}p_R\right)}\right]. \end{cases} \tag{82}$$

Once computed the pressure $p^\star$, the particle velocity $u^\star$ can be computed according to

$$u^\star(\xi) = \frac{1}{2}\left(f_R(p^\star(\xi), \mathbf{u}_R) - f_L(p^\star(\xi), \mathbf{u}_L(\xi))\right), \tag{83}$$

while the density in the star region is defined as

$$\begin{aligned} \rho_L^\star(\xi) &= \rho_L(\xi)\left(\frac{p^\star(\xi)}{p_L}\right)^{\frac{1}{\gamma}} \\ \rho_R^\star(\xi) &= \rho_R\left[\frac{\frac{p^\star(\xi)}{p_R} + \frac{\gamma-1}{\gamma+1}}{\frac{\gamma-1}{\gamma+1}\frac{p^\star(\xi)}{p_R} + 1}\right]. \end{aligned} \tag{84}$$

Now, let us determine the positions of the rarefaction wave, of the contact discontinuity and of the shock wave. In the following, HF, TF, CD and SW are used to name the head and tail of the rarefaction fan, the contact discontinuity and the shock waves respectively. These coordinates can be computed only as a function of the variable in the star region, $p^\star$ and $u^\star$, and of the left and right states $\mathbf{u}_L$ and $\mathbf{u}_R$ at a certain time t:

$$\begin{cases} \mathrm{HF}(\xi,t) = x_d - a_L(\xi)t \\ \mathrm{TF}(\xi,t) = x_d - (u^\star(\xi) - a_L^\star(\xi))t \\ \mathrm{CD}(\xi,t) = x_d + u^\star(\xi)t \\ \mathrm{SW}(\xi,t) = x_d + a_R\left[\frac{\gamma+1}{2\gamma}\frac{p^\star(\xi)}{p_R} + \frac{\gamma-1}{2\gamma}\right] \end{cases} \quad \text{where} \quad \begin{cases} a_L(\xi)^\star = a_L(\xi)\left(\frac{p^\star(\xi)}{p_L}\right)^{\frac{\gamma-1}{2\gamma}} \\ a_R = \sqrt{\gamma\frac{p_R}{\rho_R}}. \end{cases} \tag{85}$$

The complete solution of the Riemann problem is then (see also figure 20)

$$\mathbf{u}(x,\xi,t) = \begin{cases} \mathbf{u}_L(x,\xi,t) & \text{if} \quad x < \mathrm{HF}(\xi,t) \\ \mathbf{u}_F(x,\xi,t) & \text{if} \quad \mathrm{HF}(\xi,t) < x < \mathrm{TF}(\xi,t) \\ \mathbf{u}_L^\star(x,\xi,t) & \text{if} \quad \mathrm{TF}(\xi,t) < x < \mathrm{CD}(\xi,t) \\ \mathbf{u}_R^\star(x,\xi,t) & \text{if} \quad \mathrm{CD}(\xi,t) < x < sw(\xi,t) \\ \mathbf{u}_R(x,\xi,t) & \text{if} \quad x > \mathrm{SW}(\xi,t), \end{cases} \tag{86}$$

where the solution inside the rarefaction fan is as follows

$$\mathbf{u}_F(x,\xi,t) = \begin{bmatrix} \rho_L(\xi)\left[\frac{2}{\gamma+1} - \frac{\gamma-1}{a_L(\xi)(\gamma+1)}r(x,t)\right]^{\frac{2}{\gamma-1}} \\ \frac{2\rho_L(\xi)}{\gamma+1}\left[a_L(\xi) + r(x,t)\right] \\ \frac{p_L}{\gamma-1}\left[\frac{2}{\gamma+1} - \frac{\gamma-1}{a_L(\xi)(\gamma+1)}r(x,t)\right]^{\frac{2\gamma}{\gamma-1}} \end{bmatrix} = \begin{bmatrix} \rho_F(\xi) \\ m_F(\xi) \\ E^t(\xi), \end{bmatrix} \tag{87}$$

while in the star region

$$\mathbf{u}_L^\star(x,\xi,t) = \begin{bmatrix} \rho_L^\star(\xi) \\ \rho_L^\star(\xi)u^\star(\xi) \\ \frac{p^\star(\xi)}{\gamma-1} \end{bmatrix} \quad \text{and} \quad \mathbf{u}_R^\star(x,\xi,t) = \begin{bmatrix} \rho_R^\star(\xi) \\ \rho_R^\star(\xi)u^\star(\xi) \\ \frac{p^\star(\xi)}{\gamma-1} \end{bmatrix}. \tag{88}$$

A similarity variable $r(x,t)$, defined as $r(x,t) = \frac{x-x_d}{t}$, is introduced.

Note that if a value for the random parameter is fixed, the previous procedure coincide with the classical solution of the Riemann problem as reported in [24]. However, here the interest is the computations of the statistics, the expectancy and the variance, of the solution $u(x,\xi,t)$. To obtain the statistics, the solution $u(x,\xi,t)$ has to be integrated numerically splitting the random space. In particular, the integration is carried out by dividing the computational domain of the stochastic space according to (86). The complete solution of the stochastic Riemann problem for the Euler equation using the initial conditions (79), consists in capturing four structures: the region of points describing the position of the head and tail of the rarefaction wave, the contact discontinuity and the shock wave. For each zone, it is necessary to find the random parameter

$$\xi_d : x = g(\xi_d, t) \quad \forall (x,t) \in \Omega \supseteq D(t) \times T, \tag{89}$$

where the function $g(\xi,t)$ can be one of the region reported in (85). It is assumed here that functions g are monotone functions with respect to the random parameter. The subset of the physical space $D(t)$ can be defined considering the union of all the images of the functions describing the physical position of the discontinuities

$$D(t) = [\mathrm{HF}_{\min}(t), \mathrm{HF}_{\max}(t)] \cup [\mathrm{TF}_{\min}(t), \mathrm{TF}_{\max}(t)] \cup [\mathrm{CD}_{\min}(t), \mathrm{CD}_{\max}(t)] \cup [\mathrm{SW}_{\min}(t), \mathrm{SW}_{\max}(t)]. \tag{90}$$

Note that for each (x,t), more than one ξ_d corresponding to the intersections with different regions could exist, but not multiple intersections with the same region. The case of multiple intersections is determined by a non-null intersection between two or more images of the g functions. The monotonicity of the g function implies that the extrema of g correspond to the bounds of the stochastic space. This property is useful from a practical point of view because for each time step the domain $D(t)$ can be easily determined by (90).

Intersections should be computed solving the non-linear algebraic equations (89) by using Newton-Raphson techniques. Let us focus now on the four regions.

The intersection between the line x and the head fan $\mathrm{HF}(\xi,t)$ can be obtained as follows

$$x = \mathrm{HF}(\xi,t) = x_d - a_L t = x_d - \sqrt{\gamma \frac{p_L}{\rho_L(\xi)}} \quad \rightarrow \quad \rho_L(\xi) = \frac{\gamma p_L}{r^2(x,t)}. \tag{91}$$

If density ρ_L is linearly dependent on the random parameter $\xi \sim \mathcal{U}[0,1]$ (as presented in section 6.3) the value of the intersection is equal to

$$\xi_d = \frac{1}{\rho_L(1) - \rho_L(0)} \left(\frac{\gamma p_L}{r^2(x,t)} - \rho_L(0) \right). \tag{92}$$

Concerning the tail of the rarefaction wave, it follows that

$$x = x_d + \left(\frac{1}{2} \left[f_r(p^\star(\xi),\xi) - f_L(p^\star(\xi),\xi) \right] - a_L(\xi) \left(\frac{p^\star(\xi)}{p_L} \right)^{\frac{\gamma-1}{2\gamma}} \right) t \tag{93}$$

where both functions f_L and f_R are dependent on the random parameter (omitting the dependence from the left $\mathbf{u}_L(\xi)$ and right states $\mathbf{u}_R$).

The problem is to find the root of the function $F(p^\star(\xi),\xi)$

$$\begin{aligned} F(p^\star(\xi),\xi) &= r(x,t) - f_R(p^\star(\xi)) + \sqrt{\gamma \frac{p_L}{\rho_L(\xi)}} \left(\frac{p^\star(\xi)}{p_L}\right)^{\frac{\gamma-1}{2\gamma}} \\ &= r(x,t) - f_R(p^\star(\xi)) + C(p^\star(\xi),\xi) = 0, \end{aligned} \tag{94}$$

where the relation (83) is injected in the previous equation.

The iterative procedure for the solution of (94) is the following

$$\begin{cases} \Delta\xi = -\left(\dfrac{\mathrm{d}F(p^\star(\xi),\xi)}{\mathrm{d}\xi}\Big|_{\xi=\xi_k}\right)^{-1} F(p^\star(\xi_k),\xi_k)) \\ \xi_{k+1} = \xi_k + \Delta\xi, \end{cases} \tag{95}$$

where the differential is equal to

$$\begin{aligned} \frac{\mathrm{d}F(p^\star(\xi),\xi)}{\mathrm{d}\xi} &= \frac{\partial F(p^\star(\xi),\xi)}{\partial\xi} + \frac{\partial F(p^\star(\xi),\xi)}{\partial p^\star}\frac{\mathrm{d}p^\star(\xi)}{\mathrm{d}\xi} \\ &= \frac{\partial C(p^\star(\xi),\xi)}{\partial\xi} + \left(-\frac{\mathrm{d}f_R(p^\star(\xi))}{\mathrm{d}p^\star} + \frac{\partial C(p^\star(\xi),\xi)}{\partial p^\star}\right)\frac{\mathrm{d}p^\star(\xi)}{\mathrm{d}\xi}. \end{aligned} \tag{96}$$

The derivative of the function $C(p^\star(\xi),\xi)$ has to be computed as well as the derivative $\dfrac{\mathrm{d}p^\star(\xi)}{\mathrm{d}\xi}$, while $\dfrac{\mathrm{d}f_R(p^\star(\xi))}{\mathrm{d}p^\star}$ is already available (see equation (82)).

The derivatives of $C(p^\star(\xi),\xi)$ are

$$\begin{aligned} \frac{\partial C(p^\star(\xi),\xi)}{\partial\xi} &= -\frac{1}{2}\frac{\left(\frac{p^\star(\xi)}{p_L}\right)^{\frac{\gamma-1}{2\gamma}}\gamma p_L\left(\rho_L(1)-\rho_L(0)\right)}{\rho_L^2(\xi)\sqrt{\gamma\frac{p_L}{\rho_L(\xi)}}} \\ \frac{\partial C(p^\star(\xi),\xi)}{\partial p^\star} &= \frac{1}{2}\frac{\sqrt{\gamma\frac{p_L}{\rho_L(\xi)}}\left(\frac{p^\star(\xi)}{p_L}\right)^{\frac{\gamma-1}{2\gamma}}(\gamma-1)}{\gamma p^\star(\xi)}, \end{aligned} \tag{97}$$

while, at each time step, the derivative $\dfrac{\mathrm{d}p^\star(\xi)}{\mathrm{d}\xi}$ can be approximated by means of a backward difference

$$\frac{\mathrm{d}p^\star(\xi)}{\mathrm{d}\xi} \simeq \frac{p^\star(\xi_{k+1}) - p^\star(\xi_k)}{\xi_{k+1}-\xi_k}, \tag{98}$$

since $p^\star$ is not known explicitly.

From a practical point of view, the initial guess ξ_0 is chosen as the solution of the linear approximation for $\mathrm{TF}(\xi,t)$ between the extrema of the stochastic domain, with $\dfrac{\mathrm{d}p^\star(\xi_0)}{\mathrm{d}\xi} = 0.1$.

Considering the intersection with the contact discontinuity, it follows that

$$\begin{aligned} F(p^\star(\xi),\xi) &= r(x,t) - u^\star(\xi) \\ &= r(x,t) - \frac{1}{2}\left(f_R(p^\star(\xi)) - f_L(p^\star(\xi),\xi)\right) = r(x,t) - f_R(p^\star(\xi)) = F(p^\star). \end{aligned} \tag{99}$$

The iterative procedure is formally equal to (95) (even if here the dependence is not explicit with respect to ξ), with a different differential term

$$\begin{aligned}\frac{\mathrm{d}F(p^\star(\xi))}{\mathrm{d}\xi} &= \frac{\mathrm{d}F(p^\star(\xi))}{\mathrm{d}p^\star}\frac{\mathrm{d}p^\star(\xi)}{\mathrm{d}\xi}\\ &= -\frac{\mathrm{d}f_R(p^\star(\xi))}{\mathrm{d}p^\star}\frac{\mathrm{d}p^\star(\xi)}{\mathrm{d}\xi}.\end{aligned} \tag{100}$$

This differential can be computed according to (82) and (98).

Finally, the intersection with the shock waves is demanded. The non linear algebraic equation results

$$\begin{aligned}F(p^\star(\xi),\xi) &= r(x,t) - a_R\left[\frac{\gamma+1}{2\gamma}\frac{p^\star}{p_R} + \frac{\gamma-1}{2\gamma}\right]^{\frac{1}{2}}\\ &= r(x,t) - A(p^\star(\xi)) = F(p^\star(\xi)).\end{aligned} \tag{101}$$

Again, the formal iterative procedure (95) can be employed with $\frac{\mathrm{d}F(p^\star(\xi))}{\mathrm{d}\xi} = \frac{\mathrm{d}F(p^\star(\xi))}{\mathrm{d}p^\star}\frac{\mathrm{d}p^\star(\xi)}{\mathrm{d}\xi} = -\frac{\mathrm{d}A(p^\star(\xi))}{\mathrm{d}p^\star}\frac{\mathrm{d}p^\star(\xi)}{\mathrm{d}\xi}$, where

$$\frac{\mathrm{d}A(p^\star(\xi))}{\mathrm{d}p^\star} = \frac{1}{4}\frac{\gamma+1}{\gamma p_R\sqrt{\frac{(\gamma+1)p^\star(\xi)}{2\gamma p_R}+\frac{\gamma+1}{2\gamma}}}. \tag{102}$$

Let us sketch the reference solution in the plan $\xi - x$ at a final time equal to $t = 0.31$, with the initial position of the diaphragm $x_d = 0.42$ in the figure 20.

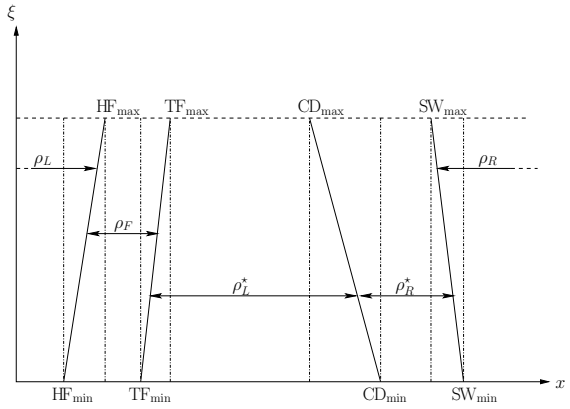

Figure 20: Schematic representation of the density of the uncertain shock tube problem in the combined physical/stochastic space. The regions where the solution should be subdivided are reported with the explicit identification of all the zones defining the variation of the solution as a function of the uncertain parameter ξ.

The expectancy of the-cell averaged physical solution (at time $t = 0.31$) $u(x,\xi,t)$, for each cell $\mathcal{C}_i = [x_i - \frac{|\mathcal{C}_i|}{2}, x_i + \frac{|\mathcal{C}_i|}{2}]$ is computed as follows (here

reported explicitly only for the density)

$$\mathcal{E}(\bar{u}_i) = \begin{cases} \dfrac{\rho_L(0)+\rho_L(1)}{2} & \text{if} \quad x_i \leq \mathrm{HF}_{\min} \\ \displaystyle\int_0^{\xi_d(x_i)} \rho_F(x,\xi)\mathrm{d}\xi + \rho_L(0)(1-\xi_d(x_i)) + \frac{(\rho_L(1)-\rho_L(0))\,(1-\xi_d^2(x_i))}{2} & \text{if} \quad \mathrm{HF}_{\min} \leq x_i \leq \mathrm{HF}_{\max} \\ \displaystyle\int_0^1 \rho_F(x,\xi)\mathrm{d}\xi & \text{if} \quad \mathrm{HF}_{\max} \leq x_i \leq \mathrm{TF}_{\min} \\ \displaystyle\int_0^{\xi_d(x_i)} \rho_L^\star(\xi)\mathrm{d}\xi + \int_{\xi_d(x_i)}^1 \rho_F(x,\xi)\mathrm{d}\xi & \text{if} \quad \mathrm{TF}_{\min} \leq x_i \leq \mathrm{TF}_{\max} \\ \displaystyle\int_0^1 \rho_L^\star(\xi)\mathrm{d}\xi & \text{if} \quad \mathrm{TF}_{\max} \leq x_i \leq \mathrm{CD}_{\min} \\ \displaystyle\int_0^{\xi_d(x_i)} \rho_L^\star(\xi)\mathrm{d}\xi + \int_{\xi_d(x_i)}^1 \rho_R^\star(\xi)\mathrm{d}\xi & \text{if} \quad \mathrm{CD}_{\min} \leq x_i \leq \mathrm{CD}_{\max} \\ \displaystyle\int_0^1 \rho_R^\star(\xi)\mathrm{d}\xi & \text{if} \quad \mathrm{CD}_{\max} \leq x_i \leq \mathrm{SW}_{\min} \\ \displaystyle\int_0^{\xi_d(x_i)} \rho_R^\star(\xi)\mathrm{d}\xi(1-\xi_d(x_i))\rho_R & \text{if} \quad \mathrm{SW}_{\min} \leq x_i \leq \mathrm{SW}_{\max} \\ \rho_R & \text{if} \quad x_i \geq \mathrm{SW}_{\max}, \end{cases} \tag{103}$$

where the variance can be computed in a similar way (see what is done for the linear advection equation §6.1 and the Burgers equation (6.2)). All the numerical quadratures are performed over the stochastic (sub-domain discretized by means of 5000 equally spaced intervals employing a three points Gauss formula:

$$\int_a^b f(\xi)\mathrm{d}\xi = \frac{b-a}{2}\sum_{k=1}^{3} w_k f(\xi_k), \tag{104}$$

where $w_{1,3} = 5/9$, $w_2 = 8/9$, $\xi_{1,3} = \frac{b+a}{2} \pm \frac{b-a}{2}\sqrt{\frac{3}{5}}$ and $\xi_2 = \frac{b+a}{2}$.

References

[1] I.G. Graham, F.Y. Kuo, D. Nuyens, R. Scheichl, and I.H. Sloan. Quasi-Monte Carlo methods for elliptic PDEs with random coefficients and applications. *Journal of Computational Physics*, 230(10):3668–3694, February 2011.

[2] Ivo Babuška, Fabio Nobile, and Raul Tempone. A Stochastic Collocation Method for Elliptic Partial Differential Equations with Random Input Data. *SIAM Review*, 52(2):317, 2010.

[3] Roger G. Ghanem and Pol D. Spanos. *Stochastic Finite Elements. A spectral approach*. Springer Verlag, 1991.

[4] Dongbin Xiu and George Em Karniadakis. Modeling uncertainty in flow simulations via generalized polynomial chaos. *Journal of Computational Physics*, 187(1):137–167, May 2003.

[5] Olivier Le Maître and O.M. Knio. *Spectral Methods for Uncertainty Quantification: With Applications to Computational Fluid Dynamics*. Springer Verlag, 2010.

[6] J Tryoen, Olivier Le Maître, M Ndjinga, and A Ern. Intrusive Galerkin methods with upwinding for uncertain nonlinear hyperbolic systems q. *Journal of Computational Physics*, 229:6485–6511, 2010.

[7] Remi Abgrall and Pietro Marco Congedo. A semi-intrusive deterministic approach to uncertainty quantifications in non-linear fluid flow problems. *Journal of Computational Physics*, (235):828–845, 2013.

[8] Rémi Abgrall, Pietro Marco Congedo, and Gianluca Geraci. An adaptive multiresolution inspired scheme for solving the stochastic differential equations. In *Proceedings of MASCOT 11, 11th Meeting on Applied Scientific Computing and Tools. Grid Generation, Approximation and Visualization. IMACS Series in Computational and Applied Mathematics Vol. 17, IAC - CNR, Rome, Italy*, pages 1–10, 2011.

[9] Rémi Abgrall, Pietro Marco Congedo, Gianluca Geraci, and Gianluca Iaccarino. Adaptive strategy in multiresolution framework for uncertainty quantification. In *Center For Turbulence Research, Prooceedings of the Summer Program 2012*, pages 209–218, 2012.

[10] R Abgrall, P M Congedo, and G Geraci. A high-order non-linear multiresolution scheme for stochastic PDEs. In *European Workshop on High Order Nonlinear Numerical Methods for Evolutionary PDEs: Theory and Applications (HONOM 2013)*, 2013.

[11] Julie Tryoen. *Methodes de Galerkin stochastiques adaptatives pour la propagation d'incertitudes parametriques dans les systemes hyperboliques*. PhD thesis, Univeriste Paris-Est.

[12] J Tryoen, Olivier Le Maître, and A Ern. Adaptive Anisotropic Spectral Stochastic Methods for Uncertain Scalar Conservation Laws. *SIAM Journal Scientific Computing*, 34:A2459–A2481, 2012.

[13] Ami Harten. Discrete multi-resolution analysis and generalized wavelets. *Applied Numerical Mathematics*, 12(13):153 – 192, 1993.

[14] Ami Harten. Adaptive multiresolution schemes for shock computations. *Journal of Computational Physics*, 135(2):260–278, August 1994.

[15] Ami Harten. Multiresolution algorithms for the numerical solution of hyperbolic conservation laws. *Communications on Pure and Applied Mathematics*, 48(12):1305–1342, 1995.

[16] Remi Abgrall and Ami Harten. Multiresolution Representation in Unstructured Meshes. *SIAM Journal on Numerical Analysis*, 35(6):2128–2146, 1998.

[17] F Arandiga and Rosa Donat. Nonlinear multiscale decompositions: The approach of A. Harten. *Numerical Algorithms*, 23:175–216, 2000.

[18] F. Arandiga, G. Chiavassa, and Rosa Donat. Harten framework for multiresolution with applications: From conservation laws to image compression. *Boletín SEMA*, 31(31):73–108, 2009.

[19] Pascal Getreuer and Francois G. Meyer. ENO multiresolutions Schemes with General Discretizations. *SIAM Journal on Numerical Analysis*, 46(6):2953–2977, 2008.

[20] R Abgrall and T Sonar. On the use of Mühlbach expansions in the recovery step of ENO methods. *Numerische Mathematik*, (1997):1–25, 1997.

[21] Alfio Quarteroni, Riccardo Sacco, and Fausto Saleri. *Matematica Numerica*. Springer, 2008.

[22] Rémi Abgrall. On Essentially Non-oscillatory Schemes on Unstructured Meshes: Analysis and Implementation. *Journal of Computational Physics*, 114(1):45–58, September 1994.

[23] R. J. LeVeque. *Finite volume methods for conservation laws and hyperbolic systems*. Cambridge University Press, 2002.

[24] E. F. Toro. *Riemann solvers and numerical methods for fluid mechanics*. Springer, Berlin, 1997.

[25] G.A. Sod. Finite Difference Methods for Systems of Nonlinear Hyperbolic Conservation Laws. *Journal of Computational Physics*, (27):1–31, 1978.

[26] Francesc Aràndiga and Ana Mara Belda. Weighted ENO interpolation and applications. *Communications in Nonlinear Science and Numerical Simulation*, 9(2):187–195, April 2004.

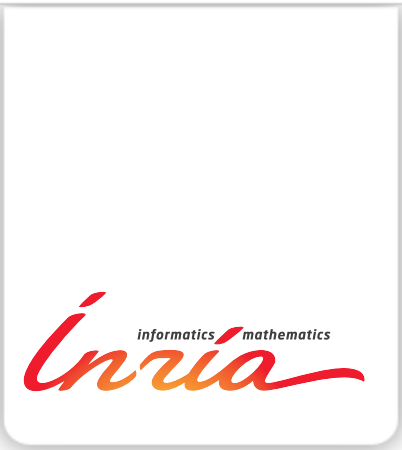

RESEARCH CENTRE
BORDEAUX – SUD-OUEST

351, Cours de la Libération
Bâtiment A 29
33405 Talence Cedex

Publisher
Inria
Domaine de Voluceau - Rocquencourt
BP 105 - 78153 Le Chesnay Cedex
inria.fr

ISSN 0249-6399